

Functional specification of CCK+ interneurons by alternative isoforms of Kv4.3 auxiliary subunits

Oláh, Viktor János^{1,2}; Lukacsovich David³; Winterer, Jochen³; Lőrincz, Andrea⁴; Nusser, Zoltan⁴; Földy, Csaba³; Szabadics, János¹

¹ Laboratory of Cellular Neuropharmacology, Institute of Experimental Medicine, Hungarian Academy of Sciences, Budapest, Hungary

² János Szentágothai School of Neurosciences, Semmelweis University, Budapest, Hungary

³ Laboratory of Neural Connectivity, Brain Research Institute, Faculties of Medicine and Natural Sciences, University of Zurich, Zurich, Switzerland

⁴ Laboratory of Cellular Neurophysiology, Institute of Experimental Medicine, Hungarian Academy of Sciences, Budapest, Hungary

Abstract

CCK-expressing interneurons (CCK+INs) are crucial for controlling hippocampal activity. We found two firing phenotypes of CCK+INs in rat CA3 area; either possessing a previously undetected membrane potential-dependent firing or regular firing phenotype, due to different low-voltage-activated potassium currents. These different excitability properties destine the two types for distinct functions, because the former is essentially silenced during realistic 8-15 Hz oscillations. The general excitability, morphology and gene-profiles of the two types were surprisingly similar. Even the expression of Kv4.3 channels were comparable, despite evidences showing that Kv4.3-mediated currents underlie the distinct firing properties. Instead, the firing phenotypes were correlated with the presence of distinct isoforms of Kv4 auxiliary subunits (KChIP1 vs. KChIP4e and DPP6S). Our results reveal the underlying mechanisms of two previously unknown types of CCK+INs and demonstrate that alternative splicing of few genes, which may be viewed as a minor event in the cells' whole transcriptome, can underlie distinct cell-type identity.

26 Introduction

27 The biophysical and morphological properties of complementary GABAergic cell classes are specifically
28 tuned for regulating the activity of the much more populous principal cells in broad temporal (from second
29 to sub-millisecond range; Hu et al., 2014, Overstreet-Wadiche and McBain, 2015) and spatial domains
30 (from axons to distal dendrites; Freund and Buzsaki, 1996). Thus, specialized features of GABAergic
31 neurons help the hippocampus to comply with the vast computational demand related to various behaviors
32 (Klausberger and Somogyi, 2008). However, the currently known degree of functional diversity of
33 GABAergic cells cannot match the vast amount of hippocampal behavioral tasks. Therefore, a more
34 complete understanding of the diversity of GABAergic neurons is one of the major goals of current
35 research. Indeed, emerging evidences from new technologies that map the complete transcriptome of
36 individual cells suggest that the number of GABAergic types may be higher than currently recognized
37 (Földy et al., 2016, Fuzik et al., 2016, Harris et al., 2018, Que et al., 2019, Tasic, 2018, Zeisel et al., 2015).
38 These new data sets accumulate a deep understanding of cellular diversity at the level of genes, which
39 requires the subsequent determination of the relation between genes and higher level complexities, such
40 as cellular excitability or morphology, which ultimately defines the distinct physiological functions of
41 individual cells. Thus, multidimensional approaches are needed for establishing links between gene level
42 diversity and the functional contribution of identified cell types. However, unanswered questions prevent
43 us from establishing links between these components. Is the diversity of different gene profiles sufficient
44 for different function, or the multitude of changes converge into similar phenotypes (Marder and
45 Goillard, 2006)? How many genes are needed for different cellular functions? To better understand the
46 boundaries of cell classes, here we employed various approaches to describe a new level of functional
47 diversity among CCK-expressing hippocampal interneurons (CCK+IN) in rat area CA3 and link this to
48 specific single cell level differences in gene profiles, expression of proteins and ionic currents.

49 Several properties distinguish CCK+INs from other major GABAergic cell classes. Unlike in other
50 GABAergic cells, the axons of CCK+INs are highly enriched with CB1 receptors, which mediate activity-
51 dependent regulation of individual synapses (Freund and Katona, 2007). As a result of this delicate
52 feedback control, CCK+INs are ideally suited for dynamic inhibition of a subset of principal cells based
53 on the context of ongoing activity. The *in vitro* firing of CCK+INs is believed to be homogeneous, regular
54 and distinct from other classes (Cea-del Rio et al., 2011, Glickfeld and Scanziani, 2006, Szabadics and
55 Soltesz, 2009, Szabo et al., 2014). The conventional view of CCK+IN firing includes intermediate AP
56 widths (between that of pyramidal cells and classical fast-spiking interneurons) and clear spike frequency

57 accommodation. These excitability properties are crucial for the generation of distinct firing of CCK+INs
58 that is observed during exploration associated with theta and gamma oscillations (Klausberger et al., 2005,
59 Lasztoczi et al., 2011) in response to specific synaptic inputs (Glickfeld and Scanziani, 2006, Matyas et
60 al., 2004). However, the CCK+IN class is diverse. Based on their axonal morphology basket-, mossy fiber-
61 associated, Schaffer collateral-associated and perforant path-associated types (Cope et al., 2002, Vida and
62 Frotscher, 2000, Vida et al., 1998) can be distinguished. These distinct morphological types selectively
63 control excitations from various sources (hence their names). Furthermore, there are molecules that are
64 complementarily expressed by subsets of CCK+INs, such as VGluT3 and VIP (Somogyi et al., 2004) and
65 single-cell RNA-sequencing also uncovered several additional molecular varieties (Fuzik et al., 2016).
66 Thus, due to their distinction from other major classes and large interclass variability, CCK+INs are ideal
67 for addressing general questions concerning the relation of genes to cellular identity and boundaries
68 between GABAergic cell classes.

69 In this study, we investigated hippocampal CCK+INs from a broader perspective that could reveal
70 previously undetected excitability parameters suitable for specific physiological functions. A hint that
71 such diverse physiological parameters exist came from previous *in vivo* recordings that showed that
72 individual CCK+INs are differentially active during various oscillatory states (Klausberger et al., 2005,
73 Lasztoczi et al., 2011), where many of them appeared to prefer either lower or higher frequency ranges.
74 We found two types of hippocampal CCK+INs in rats based on their different excitability, with potentially
75 different contributions to network events, particularly in the range of theta oscillations. Detailed realistic
76 simulations showed that switching only the properties of Kv4.3-mediated currents can sufficiently convert
77 one functional cell type to the other. Combined analyses of the complete mRNA content and protein
78 expression of single cells revealed that the pronounced functional distinction between the here-described
79 two CCK+IN type is defined by differential isoform usage of three auxiliary subunits of the Kv4.3
80 channels.

81 Results

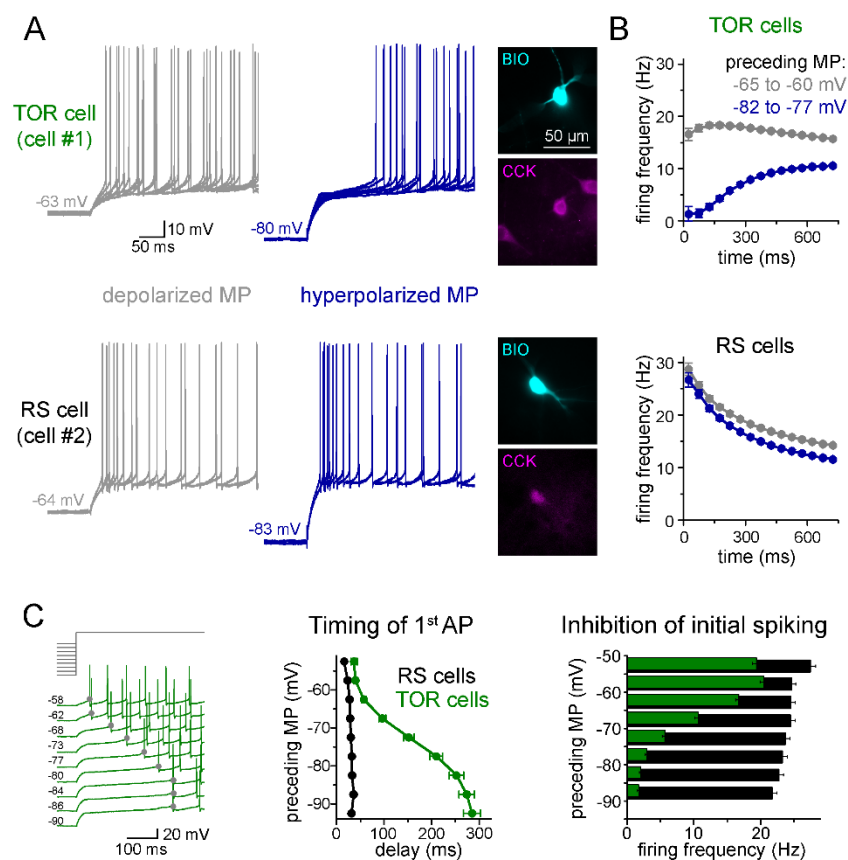
82 Half of the CA3 CCK+INs show state-dependent firing

83 To explore potential differences in the excitability of individual CCK+INs in the CA3 region of the rat
84 hippocampus, first we characterized their firing properties in two different conditions. Specifically, we
85 recorded their spiking in response to current steps from two, physiologically plausible membrane potential
86 ranges of *post hoc* identified CCK+INs. We focused mostly on CA3 region because CA3 CCK+INs are
87 the most diverse within the hippocampus. When CCK+INs ($n = 557$ cells) were stimulated from slightly
88 depolarized membrane potentials (MP, range: $-60 - -65$ mV) relative to rest (-64.7 ± 0.4 mV), action
89 potential (AP) firing always showed spike-frequency accommodation, which is one of the most
90 characteristic features of this cell class (Cea-del Rio et al., 2011, Glickfeld and Scanziani, 2006, Szabadics
91 and Soltesz, 2009, Szabo et al., 2014). However, we noticed that numerous CCK+INs ($n = 290$ cells)
92 showed MP-dependent firing: their initial spiking was strongly inhibited and its onset was delayed when
93 it was evoked from hyperpolarized MPs (between -75 to -85 mV, [Figure 1A-B](#)). On average, these cells
94 started firing after a 252 ± 15 ms silent period from hyperpolarized MP (measured from the start of the
95 current injection). We categorized these cells as Transient Outward Rectifying cells or TOR cells (a term
96 that was used to describe cells in other brain regions: Stern and Armstrong, 1996). The rest of CCK+INs
97 ($n = 267$ cells) were characterized as regular spiking or RS cells as they fired regularly irrespective of their
98 MP and they started firing with a short delay (33 ± 2 ms) when stimulated from hyperpolarized MP. At
99 depolarized MP (-55 to -65 mV), the first APs of both TOR and RS cells occurred with short delays (48
100 ± 3 ms and 26 ± 1 ms, respectively, *Student t-test*, $p = 0.09$, $t(160) = -1.706$).

101 Next, we applied a protocol allowing the detailed quantification of the MP-dependence of firing in
102 individual cells ($n = 81$ RS and 85 TOR cells). Specifically, firing was evoked by a current step that was
103 calibrated for each cell to elicit similar average firing (10 - 20 Hz) from slightly depolarized MP. The
104 holding current preceding the standard step was systematically varied to reach a wide range of steady-
105 state MPs (3 seconds, in the range of -50 and -90 mV, [Figure 1C](#)). In TOR cells, the number of APs within
106 the first 150 ms and the timing of the first AP showed steep voltage dependence ($V_{1/2}$ value of the
107 Boltzmann fits were -67.4 mV and -73 mV, respectively, $R^2 = 0.995$ and 0.999 , [Figure 1C](#)). In contrast,
108 the delay and number of spikes did not show membrane potential-dependence in RS cells.

109 Unlike the initial spiking, the general firing and membrane properties of TOR and RS cells were similar,
110 including input resistance (143 ± 7 M Ω vs. 139 ± 7 M Ω , $n = 112$ TOR and $n = 122$ RS cells, respectively),
111 AP threshold (-37.4 ± 0.4 mV vs. -37.6 ± 0.4 mV), AP half-width (0.49 ± 0.01 ms vs. 0.51 ± 0.01 ms),

112 dV/dt maximum (484 ± 13 mV/ms vs. 486 ± 14 mV/ms) and AHP amplitude (-15.5 ± 0.3 mV vs. $-14.4 \pm$
 113 0.3 mV). Furthermore, the frequency of spontaneous synaptic events (including both IPSCs and EPSCs;
 114 2.47 ± 0.57 Hz and 3.26 ± 0.86 Hz, $n = 9$ TOR and 8 RS cells) and amplitude of these events (-51.6 ± 3.3
 115 pA and -51.5 ± 2.5 pA) were also similar. TOR cells were present in the CA1 region as well. However,
 116 here their prevalence was lower compared to CA3 (2 TOR out of 13 CA1 CCK+IN). Both TOR ($n = 15$
 117 cells) and RS ($n = 12$ cells) CCK+INs were also detected in the CA3 region of adult rats (older than 70
 118 days). In summary, the firing of TOR cells shows a remarkable sensitivity to a physiologically plausible
 119 20 mV shift in the MP, despite having no other distinctive passive electrical or spiking properties
 120 compared to RS cells.



121

122 **Figure 1. Two distinct firing patterns within CA3 CCK+ cells.**

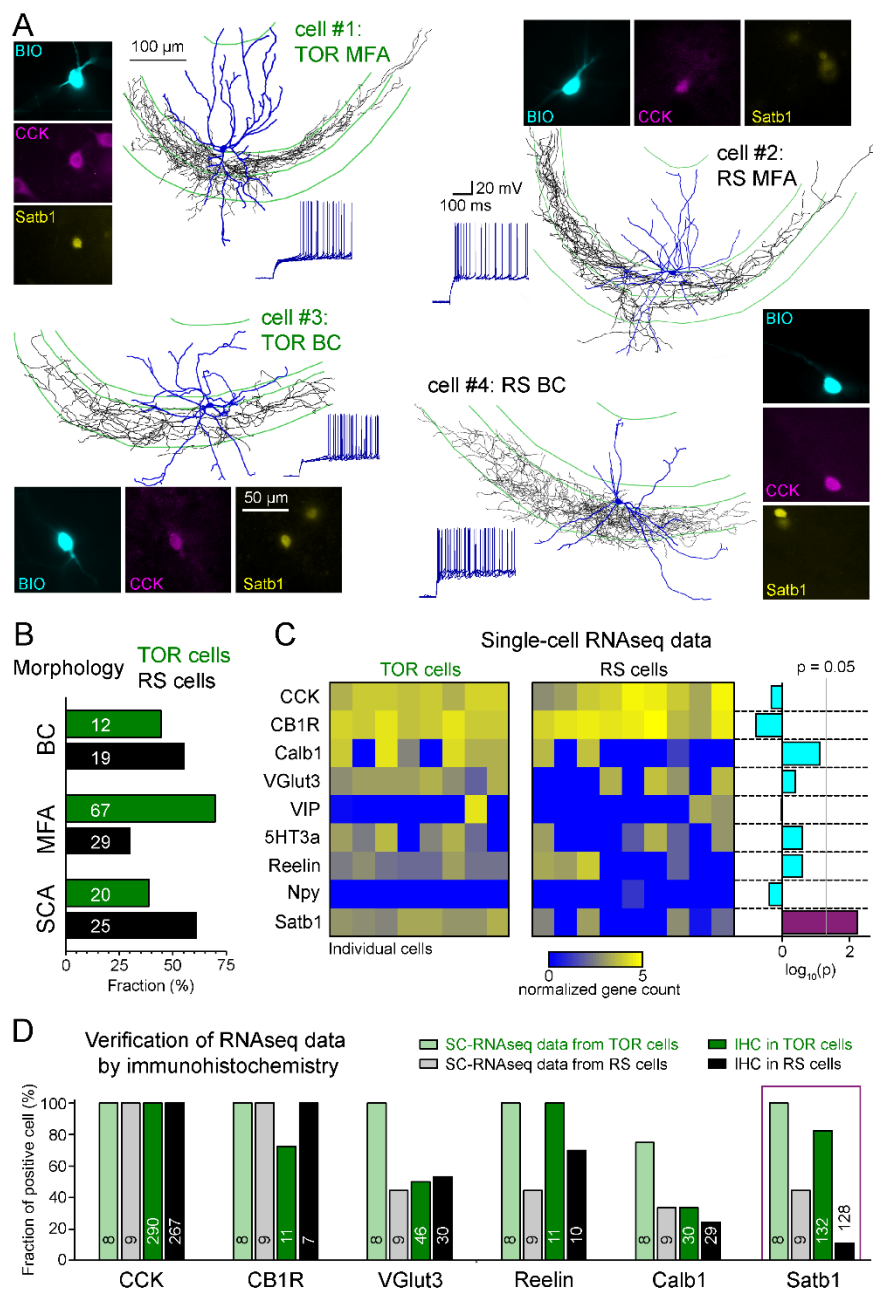
123 **A.** Firing properties of two representative CCK+INs in the CA3 hippocampal region. Firing was elicited with square
 124 pulse current injection of identical amplitude, but from depolarized (grey traces), or hyperpolarized MPs (blue
 125 traces). Several trials are superimposed to show the stability of the timing of the first action potential. Insets show
 126 the immunolabelling of the biocytin filled (BIO) recorded cells for CCK. **B.** Average time course of AP occurrence
 127 in TOR and RS cells from two MP ranges ($n = 120$ and 113 representative cells, respectively). **C.** Timing of the
 128 first AP and probability of APs during the first 150 ms of the square pulse stimulus shows steep MP-dependence in
 129 TOR cells, whereas the initial spikes are stable in the RS cells. The amplitude of stimulating current steps was

130 standardized for each cell and only the preceding holding current (3 seconds) was varied in individual trials. Traces
131 show a representative recording from a TOR cell. The average data derived from 85 TOR and 81 RS cells.
132

133 **TOR and RS firing types do not correlate with previously known subtypes of CCK+** 134 **cells**

135 The CCK+IN class has been previously divided into several subtypes based on various functionally
136 relevant features. Therefore, next we investigated whether the two MP-dependent firing phenotype can be
137 linked to previously known subtypes of CCK+INs. Three subtypes have been previously identified within
138 CA3 CCK+INs based on the target zones of their axons. Basket cells (BCs) innervate the soma and
139 proximal dendrites (Hendry and Jones, 1985). Mossy fiber-associated (MFA) cells are specific to the CA3
140 region where their axons colocalize with the axons of dentate gyrus granule cells in stratum lucidum and
141 hilus (Vida and Frotscher, 2000). The third morphological type is named after the position of their axons
142 as Schaffer collateral associated cells (SCA)(Cope et al., 2002). Altogether, 172 of the recorded CCK+INs
143 were unequivocally identified either as BCs (n = 31), MFAs (n = 96) or SCAs (n = 45; [Figure 2A](#)). Both
144 TOR and RS firing types occurred similarly among these morphological subtypes ([Figure 2B](#)) indicating
145 that the two firing phenotypes cannot be assigned to these morphology-based subtypes of CCK+INs.

146 In addition to the variable axonal morphology, CCK+INs are known to heterogeneously express several
147 molecules (Somogyi et al., 2004). To compare their molecular content first we performed single cell RNA
148 sequencing (SC-RNAseq) (Földy et al., 2016) of individually recorded TOR cells (n = 8) and RS cells (n
149 = 9). Only those cells were analyzed in detail, which had detectable mRNA for both CCK and
150 cannabinoid-receptor type 1 (CB1R or Cnr1; [Figure 2C](#)). In accordance with previous observations (Földy
151 et al., 2016), the included cells contained the transcripts of at least 3000 different genes. Most subtype-
152 specific marker genes (calbindin/Calb1, vesicular glutamate transporter VGlut3/slc17a8, vasoactive
153 intestinal protein/VIP, serotonin receptor subtype 3a/5HT3a, Reelin, neuropeptide-Y/Npy) were present
154 at comparable levels in TOR and RS cells ([Figure 2C](#)), except the activity-dependent transcription
155 regulator, Satb1 (Close et al., 2012). All tested TOR cells had high levels of Satb1 mRNA, whereas it was
156 present only in 4 of the 9 tested RS cells (*Mann-Whitney test, p = 0.0058, z = 2.76, U = 65*). Furthermore,
157 to compare the general gene profiles, we performed hierarchical cluster analysis based on all genes that
158 were detected in at least 3 of the 17 tested cells (10095 out of 30662 tested genes, data not shown). This
159 analysis did not categorize these cells into two distinct groups that would correspond to their firing
160 phenotype, arguing for their similar cell class identity (Fuzik et al., 2016, Harris et al., 2018).



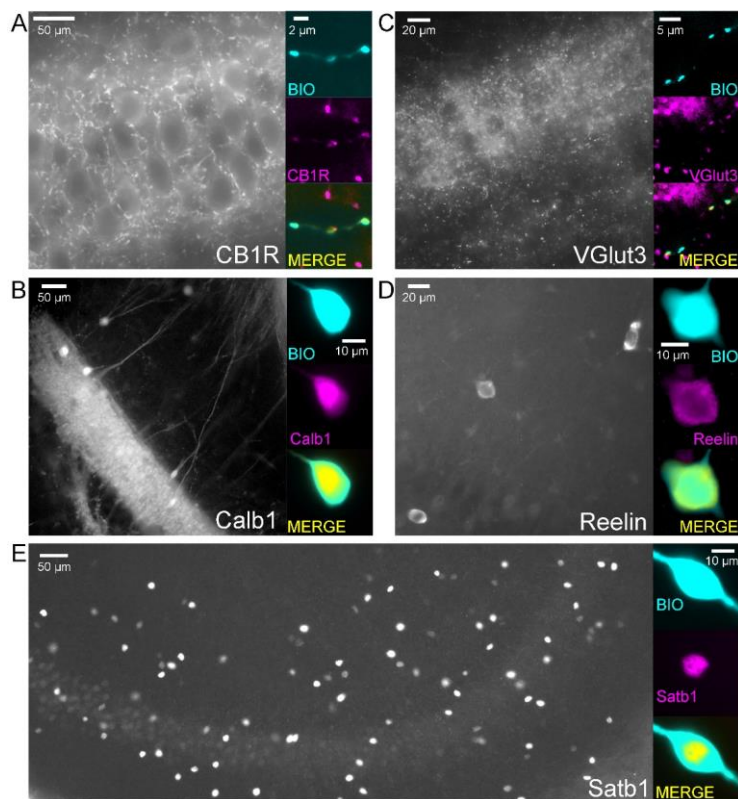
161

162 Figure 2. Different excitability does not correlate with previously known diversity of CCK+ cells.

163 A. Axonal (black) and dendritic (blue) reconstructions of four CCK+INs in the CA3 region representing two major
 164 morphological types, the mossy-fiber associated cells and basket cells. The firing of cell#1 and #2 are shown in
 165 detail in Figure 1A. The firing from hyperpolarized MP is shown for each cell. Immunolabellings for CCK and the
 166 nuclear protein Satb1 are shown next to each recorded cell. B. Prevalence of TOR and RS cells within three major
 167 morphological types of CA3 CCK+. Numbers of identified cells are indicated on each bar (BC: CCK+ basket cells,
 168 MFA: mossy-fiber associated cells, SCA: Schaffer-collateral associated cells). C. Single cell RNAseq
 169 characterization of recorded TOR (left, n = 8) and RS (right, n = 9) cells for known GABAergic cell markers. Each
 170 column corresponds to single identified CCK+INs. Only Satb1 mRNA content was significantly different between
 171 TOR and RS cells ($p = 0.00346$, Mann-Whitney Test). D. Comparison of immunohistochemical and single cell
 172 RNAseq data. Bar plots show the fraction of the recorded cells with detectable RNA content (threshold: 0.2) for the

173 selected markers and immunopositivity for the same proteins (for examples of the immunolabelling see [Figure 2–](#)
174 [figure supplement 1](#)). The number of tested cells are shown on each bar.
175

176 To confirm these findings at the level of protein expression, next we performed immunohistochemistry
177 on identified CCK+ TOR and RS cells in separate experiments ([Figure 2D](#) and [Figure 2 - figure](#)
178 [supplement 1](#)). As expected, CB1R protein was detected in the axon of almost all tested cells (15 out of
179 18 tested cells). Furthermore, VGluT3 (23 out of 46 TOR cells, 16 out of 30 RS cells), Reelin (all TOR,
180 n = 11 and 7 out 10 RS was positive) and Calb1 (10 out 30 TOR and 7 out of 29 RS) proteins occurred
181 similarly in RS and TOR types. However, the majority of the tested TOR cells were positive for Satb1
182 protein (109 out of 132, 82.6%) but only few RS cells were positive (14 out of 128 tested, 10.9%). Satb1
183 protein was also prevalent in non-recorded CCK+ cells within the CA3 region of the acute slices (126
184 Satb1+/CCK+ out of 425 CCK+), suggesting that the presence of this activity-dependent marker is not
185 due to the recording. The somata of Satb1+/CCK+ cells were found throughout CA3 strata oriens,
186 pyramidale, lucidum and radiatum and their proportion to all CCK+ cells were variable (34.1%, 21.4%,
187 33.6%, and 27.2%, respectively). In agreement with the lower occurrence of TOR cells in the CA1, non-
188 recorded CCK+ cells in this region were less likely to be Satb1 positive (21.6% of 231 CCK+ cells). In
189 the hilar region of the dentate gyrus the proportion of Satb1+/CCK+ cells was also low (4.8% of 123
190 CCK+ cells). We have also detected Satb1 and CCK overlap in tissue samples derived from transcidentally
191 perfused animals (20.2%, 97 Satb1+/CCK+ out of 480 CCK+ cells in the CA3 area). Thus, the mRNA
192 and immunohistochemical data suggest that the Satb1 content of hippocampal CCK+INs is predictive for
193 their TOR or RS identity and these firing phenotypes are not related to previously known subtypes of the
194 CCK+IN class.



195

196 **Figure 2 – figure supplement 1.**

197 Example cells that were immunopositive for CB1R (A), Calb1 (B), VGlut3 (C), Reelin (D) and Satb1 (E) and the
198 low magnification overview of the labeling pattern of these molecules within the CA3 region.

199

200 **Differences in low-voltage-activated potassium currents (I_{SA}) underlie the**
201 **heterogeneity of CCK+IN firing**

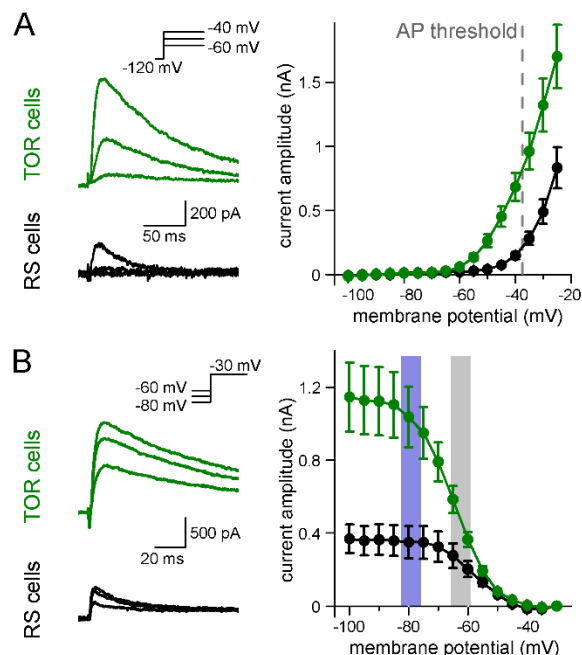
202 Next, we investigated the conductances that are responsible for the difference of the two firing types in
203 CCK+INs. We focused on near-threshold potassium currents, which can effectively regulate firing
204 responses in similar experimental conditions in various brain regions (Lammel et al., 2008, Margrie et al.,
205 2001, Neuhoff et al., 2002, Stern and Armstrong, 1996). First, we characterized each cell as TOR or RS
206 type under normal recording conditions. Then, we blocked sodium (3 μ M TTX) and hyperpolarization-
207 activated cation currents (10 μ M ZD7288) and recorded near-threshold potassium currents by applying
208 300 ms voltage command steps between -100 and -25 mV from -120 mV conditioning potentials (300
209 ms). All cells included in the analyses were verified to be CCK+ by *post hoc* immunolabelling. TOR cells
210 had a substantial amount of potassium currents at firing threshold ([Figure 3A](#), 683 ± 109 pA at -40 mV).
211 In contrast, potassium currents in RS cells activated at more positive voltages and were much smaller at
212 threshold (148 ± 28 pA, $p = 0.0006$, $t(26)=3.885$, $n = 17$ and 11 , *Student's t-test*). Because in these

213 recording conditions the majority of the membrane conductances remained intact, voltage clamping could
214 not be properly performed at more depolarized MPs, which precluded the determination of the exact half-
215 activation voltage values. The robust low-voltage-activated potassium currents (I_{SA}), which are activated
216 tens of millivolts below AP threshold, can underlie the strong inhibition of AP generation in TOR cells
217 whereas I_{SA} in RS cells is much smaller at near-threshold voltage range.

218 Next, we investigated the availability of I_{SA} at different MPs. For these measurements, potassium currents
219 were evoked by a voltage step to -30 mV following various pre-pulse potentials between -100 to -35 mV.
220 The $V_{1/2}$ of the average inactivation curve was -64.5 ± 0.2 mV (*Boltzmann fit*, $R^2 = 0.999$, mean of $V_{1/2}$
221 from individual cells: -63.8 ± 0.9 mV, $n = 13$ cells, [Figure 3B](#)) in TOR cells. Importantly, the majority of
222 I_{SA} was available at slightly hyperpolarized MPs ($91.3 \pm 1.6\%$ at -80 mV), where the inhibition of firing
223 was clearly observable during the characterization of TOR cells (see [Figure 1](#) data). But at -60 mV, where
224 the inhibition of spiking was not prominent, the majority of outward currents in TOR cells were
225 inactivated; only $35.7 \pm 3.4\%$ of the current was available. Thus, the MP-dependence of the steady-state
226 inactivation of I_{SA} can explain the TOR firing phenotype. Similar to the activation, the inactivation of I_{SA}
227 in RS cells was shifted toward positive voltage ranges ($V_{1/2}$: -57.4 ± 0.3 mV, $n = 8$ cells, mean of individual
228 data: -55.6 ± 2 mV, comparison with TOR cells: $p = 0.0006$, $t(19)=4.12$, *Student's t-test*) and a larger
229 portion of this smaller current was available at -60 mV ($52.7 \pm 6.3\%$, [Figure 3B](#)). Thus, hyperpolarization
230 of the RS cells cannot add a substantial amount of AP-firing disabling inhibitory conductance.

231 Interestingly, the inactivation time constant of I_{SA} was faster in RS cells compared to TOR cells ($18.8 \pm$
232 1.7 ms vs. 71.2 ± 9.1 ms, measured at -25 mV, $p = 0.0007$, $t(19)=4.025$, *Student's t-test*, $n = 7$ and 14).
233 Furthermore, the recovery from inactivation was faster in RS cells, but it showed steep voltage dependence
234 in TOR cells (TOR cells: time constants of the recovery were 58.2 ± 2.9 ms, 46.2 ± 2.9 ms, 29.8 ± 2.5 ms
235 and 4.4 ± 0.1 ms at -65, -75, -85 and -120 mV, respectively; whereas in RS cells: 11.8 ± 4.4 ms, 8.0 ± 2.2
236 ms, 7.1 ± 1.6 ms and 3.3 ± 0.4 ms, respectively). Due to these properties, I_{SA} currents in RS cells resulted
237 in only a small inhibitory charge transfer around the AP threshold, whose availability remains similarly
238 limited within the relevant -80 and -60 mV MP range. Thus, the different properties of I_{SA} currents,
239 particularly the left-shifted inactivation and activation curves, can explain the differences in TOR and RS
240 firing phenotypes.

241



242

243 **Figure 3. Differences in I_{SA} currents underlie the heterogeneity of CCK+IN firing.**

244 **A.** Representative traces of low voltage activated potassium currents from TOR and RS cells (in the
245 presence of 3 μ M TTX and 10 μ M ZD7288). Right, voltage dependence of activation of I_{SA} in TOR (n =
246 17) and RS (n = 11) cells. The grey dotted line indicates AP threshold (-37.52 ± 0.3 mV) measured before
247 TTX application. Notice the large amount of outward current in TOR cells at subthreshold MPs. **B.**
248 Representative traces of I_{SA} activated at -30 mV from different holding potentials. Right, voltage
249 dependence of inactivation of I_{SA} in the two cell types (n = 14 and 10 for TOR and RS cells respectively).
250 Blue and grey shaded areas indicate the voltage ranges from which state-dependent firing was tested (see
251 [Figure 1](#)).
252

252

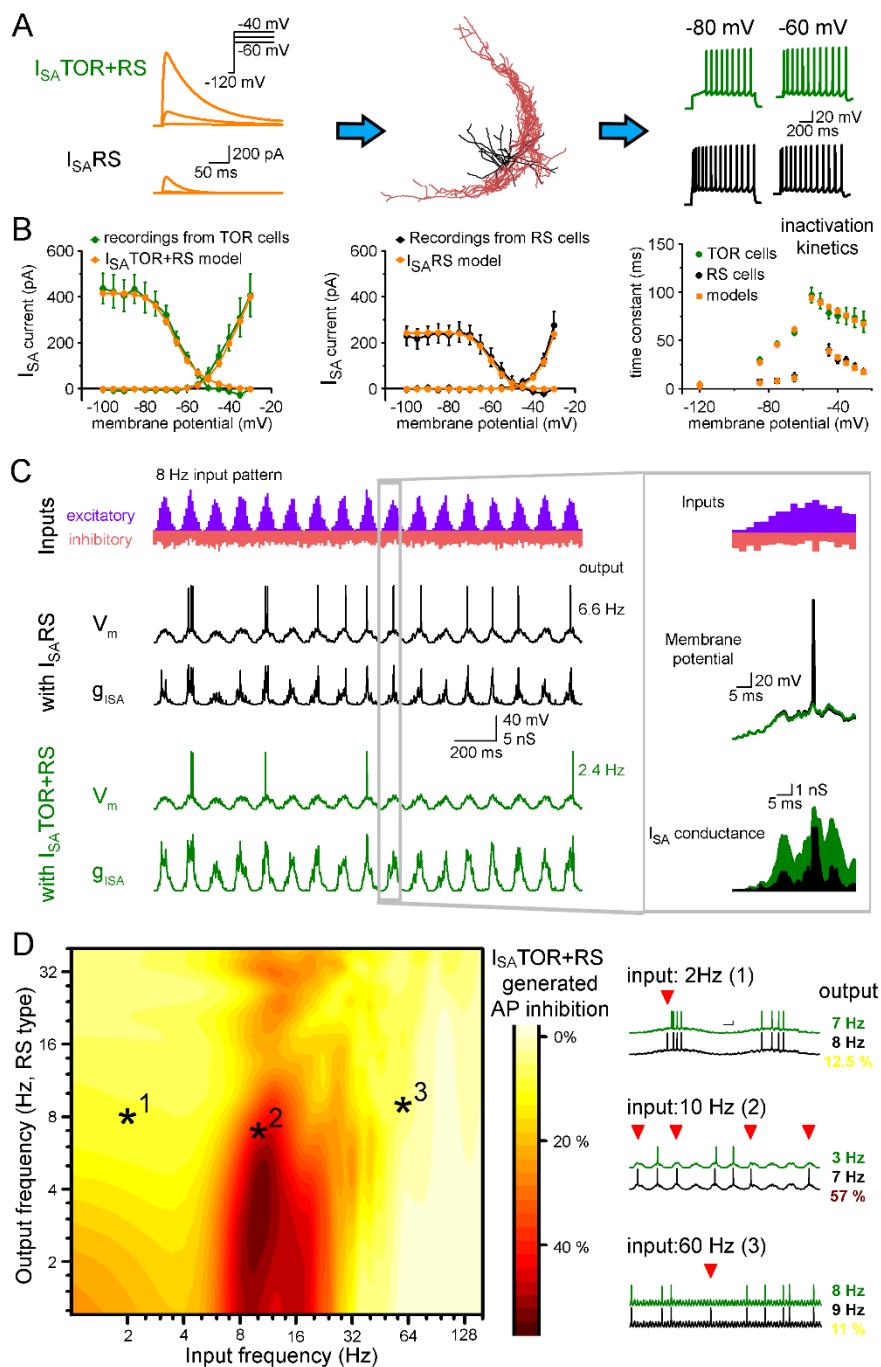
253 **Realistic models of TOR and RS firing**

254 In the previous experiments, we injected simple steady-state currents to CCK+INs, which already revealed
255 remarkably different excitability properties. However, excitation of neurons *in vivo* is more dynamic due
256 to the fast rise and decay of PSPs that are clustered into packages according to the ongoing oscillatory
257 state of the network, resulting in a constantly fluctuating membrane potential. The different temporal
258 properties of I_{SA} in TOR and RS suggest that these cells can follow membrane potential fluctuations
259 differently. Therefore, to predict the frequency ranges of oscillations that are optimal for the distinct
260 CCK+IN types with distinct excitability, we performed computer simulations of realistic dynamic
261 behavior of RS and TOR phenotypes.

262 First, we equipped five reconstructed CCK+INs (3 TOR and 2 RS types) with known voltage-dependent
263 conductances and passive properties of hippocampal CCK+INs (Bezaire et al., 2016) and reproduced the

264 general firing properties ([Figure 4A](#)). To add the I_{SA} currents to the models, we recorded the properties of
265 local I_{SA} current by pulling outside-out patches from the soma and dendrites of RS and TOR cells ([Figure](#)
266 [4 – figure supplement 1A-B](#)). This additional experiment was necessary because the subcellular
267 distribution of many ion channels are inhomogeneous (Nusser, 2009), which also influences the
268 somatically measured ensemble currents. I_{SA} was isolated by subtraction of currents measured at 0 mV
269 with -80 and -50 mV pre-pulses. We did not observe a significant gradient along the dendritic axis of the
270 two cell types, albeit there was a tendency for larger somatic current densities compared to dendrites. The
271 average kinetics of patch currents matched those of whole-cell currents: slower inactivation in TOR
272 cells/patches. However, we detected a large variability of I_{SA} between individual patches from TOR cell
273 ([Figure 4 – figure supplement 1C](#)), even when multiple patches were pulled from the same cell. Patches
274 from RS cells were more homogeneous (variance of current decays, TOR: 2888 ms², RS: 373 ms²).
275 Surprisingly, in many TOR cell patches the current kinetics resembled the patch- and whole-cell currents
276 of the RS cells. While in other TOR cell patches much slower currents were also detected. This variability
277 might be due to the clustered occurrence of voltage-gated potassium channels in GABAergic cells (e.g.
278 see Kollo et al., 2006). We implemented this variability by equipping TOR models with two types of I_{SA}
279 currents (for details see below).

280 These outside-out patch recordings also allowed us to directly compare the density of I_{SA} in TOR and RS
281 cells because the majority of channels are expected to be open at larger voltage steps (to 0 mV) and the
282 current amplitude is determined by the driving force and the conductance. Interestingly, the density of
283 somatic I_{SA} in RS cells were significantly larger compared to that of the TOR cells (70.5 ± 15.2 pA/ μm^2
284 vs. 42.2 ± 5.2 pA/ μm^2 , $n = 26$ and 17 , $p = 0.047$, $t(41) = -2.048$). This result does not contradict with the
285 above data that the total I_{SA} current is larger in TOR cells near the AP threshold because in TOR cells the
286 activation of I_{SA} is left-shifted, therefore, a larger fraction of channels is open at lower voltages. In
287 dendritic patches (25-320 μm) the density of I_{SA} was similar in TOR and RS cells (19.6 ± 3.3 pA/ μm^2 vs.
288 19.5 ± 3.0 pA/ μm^2 , $n = 53$ and 47).

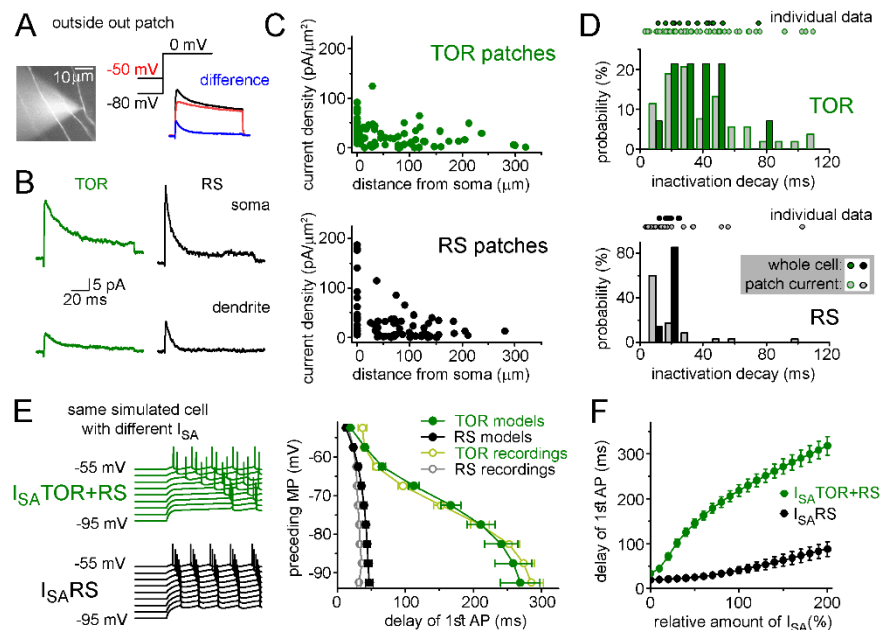


289

290 **Figure 4. Different I_{SA} currents in TOR and RS cells tune them for different network states.**

291 **A.** I_{SA}^{TOR+RS} and I_{SA}^{RS} were added to five reconstructed CCK+INs, which possess every known voltage-
 292 voltage-dependent conductance (Bezaire et al., 2016). Changing I_{SA}^{RS} to I_{SA}^{TOR+RS} in the same cells transformed the
 293 firing from RS to TOR phenotype. These simulated cells were equipped with synaptic conductance to simulate
 294 input drives in various network states. **B.** Voltage clamp simulations with complete morphology and realistic
 295 conductances reproduced whole-cell I_{SA} currents of TOR and RS cells, including voltage-dependence, the total
 296 current measured at the soma (left and middle graphs), and inactivation and the kinetics of inactivation and recovery
 297 from inactivation (right graph, where recovery was measured at -120, -85, -75 and -65 mV). Note that the total
 298 amount of I_{SA} in RS cells was larger than in TOR cells (Figure 4 – figure supplement 1A-C) and the larger current

299 at low voltages are the consequence of the left-shifted activation curve. **C.** Representative traces showing the
 300 number and temporal distribution of 8 Hz-modulated synaptic inputs a simulated CCK+INs and its MP and I_{SA}
 301 conductance in two conditions with either $I_{SA}RS$ or $I_{SA}TOR+RS$. **D.** Average effects of exchanging $I_{SA}RS$ to
 302 $I_{SA}TOR+RS$ on the output of five CCK+INs during various input frequency ranges (x-axis) and baseline output
 303 activity (i.e. with $I_{SA}RS$ conductance, y-axis). Yellow color shows no change in firing when $I_{SA}TOR+RS$ replaced
 304 $I_{SA}RS$, whereas red color indicates robust reduction in AP output. Representative traces on the right depict three
 305 examples with different input frequencies. Red triangles highlight inhibited spikes.
 306



307

308 **Figure 4 – figure supplement 1. Realistic CCK+INs in-silico.**

309 **A.** Representative outside-out patch recording of dendritic I_{SA} current from a RS cell, which was somatically loaded
 310 with Alexa594 dye to visualize dendrites in epifluorescent illumination and to record firing pattern. I_{SA} current
 311 (blue) was evoked at 0 mV and isolated by subtracting currents evoked with -80 mV prepulse voltage from -50 mV
 312 prepulse. **B.** Average I_{SA} currents from somata and dendrites of RS and TOR cells ($n = 22$ somatic TOR-, $n = 17$
 313 somatic RS-, $n = 56$ dendritic TOR and $n = 53$ dendritic RS patches). **C.** Current densities are plotted against
 314 dendritic distance. Current densities were calculated by dividing the peak of I_{SA} current with the membrane surface
 315 of the patch, which was calculated from the capacitance difference measured with the patch membrane and after
 316 pushing the pipette in an insulator gel (Sylgard). **D.** Comparison of inactivation decay time constants of I_{SA}
 317 measured in individual whole-cell and outside-out recordings (TOR patch: 74.5 ± 7.4 ms, variance: 2888, $n = 53$;
 318 TOR whole-cell, 71.2 ± 9.1 ms, variance: 1147, $n = 14$, RS patch: 17.2 ± 3.3 ms, variance: 373, $n = 35$). Symbols
 319 above the graphs show individual measurements and their distributions are represented by bar graphs. Notice the
 320 wider distribution of patch data compared to whole-cell data from TOR cells. **E.** Left, representative current-clamp
 321 simulations from a single model cell with either $I_{SA}TOR+RS$ or $I_{SA}RS$ currents. Notice the characteristic MP-
 322 dependence of spike onset with $I_{SA}TOR+RS$. The graph on the right summarizes the MP-dependence of timing of
 323 the first APs from five model cells with either $I_{SA}TOR+RS$ or $I_{SA}RS$. The results from recordings using the same
 324 protocols are shown for comparison (from [Figure 1C](#), open symbols). **F.** Conductance density has little effect on
 325 the presence or absence and the extent of the TOR phenomenon suggesting that the kinetic and voltage-dependent
 326 properties of the two sets of I_{SA} currents play a more important role in this phenomenon than the amounts of
 327 inhibitory conductance (measured from -80 mV preceding MP).

328 Based on the results of the above recordings, we used two sets of I_{SA} conductances and tuned their densities
329 to recreate RS and TOR firing properties in simulations. In the model, the recorded whole-cell I_{SA}
330 potassium currents and firing properties were best represented if RS cells were equipped with a single
331 type of I_{SA} potassium conductance ($I_{SA}RS$). Whereas, I_{SA} currents of TOR cells were reproduced by a
332 mixture of two I_{SA} potassium conductances, including $I_{SA}RS$ and a left-shifted, slowly inactivating current
333 ($I_{SA}TOR$) in a 3:1 ratio. This mixed I_{SA} ($I_{SA}TOR+RS$) is not only consistent with the variability of the
334 patch current kinetics but also reproduces the properties of whole-cell currents ([Figure 4B](#)). After adding
335 $I_{SA}RS$ or $I_{SA}TOR+RS$ to the core CCK+IN properties (Bezaire et al., 2016) in current-clamp simulations,
336 the models reproduced the common firing properties of CCK+INs (including AP width, peak and
337 frequency and AHP shape), but in the presence of $I_{SA}TOR+RS$ all five cells showed MP-dependent firing
338 with similar temporal dynamics and voltage dependence as recorded experimentally. When the same cells
339 were equipped with $I_{SA}RS$ only, they turned to RS firing type ([Figure 4 – figure supplement 1E-F](#)). Thus,
340 exchange of $I_{SA}RS$ to $I_{SA}TOR+RS$ alone is sufficient to generate TOR properties, even if the reconstructed
341 cell originally belonged to the RS type and vice versa.

342 Surprisingly, these results also suggest that TOR firing required much less (57.5%) I_{SA} potassium
343 conductance in total, than RS firing in the same reconstructed cells. This could be an additional
344 consequence of the left-shifted activation of I_{SA} in TOR cells (further supports for this argument will
345 follow below).

346

347 **TOR cells are selectively silenced by $I_{SA}TOR$ in a narrow range of oscillatory states**

348 Next, we simulated the activity of RS and TOR firing cells during *in vivo*-like oscillating network
349 conditions using excitatory and inhibitory inputs arriving onto the somato-dendritic axis of the five models
350 of CCK+INs. The occurrence of excitatory events was clustered and tuned to frequencies ranging from 1
351 to 100 Hz and their kinetics were deducted from recordings from CCK+INs (see Methods). All five cells
352 received the same input patterns and the strengths of excitation was varied (by changing the number of
353 EPSCs, [Figure 4C](#)), which resulted in a wide range of spiking frequencies in CCK+INs representing the
354 frequency ranges that have been recorded *in vivo* (Klausberger et al., 2005, Lasztocki et al., 2011).

355 Next, we compared the average spiking of $I_{SA}TOR+RS$ potassium conductance-equipped CCK+INs (n =
356 5 cells) with the spiking of the same cells during the same conditions except that they were equipped only
357 with $I_{SA}RS$. As [Figure 4](#) panel D shows, in most conditions, the presence of $I_{SA}TOR+RS$ instead of $I_{SA}RS$
358 did not markedly reduce the firing rates. However, CCK+INs were efficiently silenced by $I_{SA}TOR+RS$ in

359 8-15 Hz input frequency regimes. On average, $39.1 \pm 0.6\%$ fewer APs were evoked (see red areas in the
360 middle of the [Figure 4D](#) graph and example traces). In contrast, during lower and higher input regimes
361 the presence of $I_{SA}TOR+RS$ reduced firing only slightly (spiking was decreased by $8 \pm 0.3\%$ and $7.5 \pm$
362 0.2% , between 1-6 Hz and 25-100 Hz).

363 Thus, the results of these simulations suggest that $I_{SA}TOR+RS$ conductance alone enables CCK+INs to
364 be selectively silenced during 8-15 Hz input regime, which adds a novel level of complexity to the diverse
365 functions of GABAergic cells and can contribute to their observed heterogeneous firing during different
366 network states (Klausberger et al., 2005, Klausberger and Somogyi, 2008, Lasztocki et al., 2011). The
367 input frequency dependence of the inhibition of firing can be explained by the specific temporal properties
368 of $I_{SA}TOR+RS$. Specifically, in addition to the voltage dependence of activation and inactivation ([Figure](#)
369 [3](#)), the time constant of inactivation ([Figure 4 – figure supplement 1D](#)) and the recovery from inactivation
370 determines the different availability of these currents during various oscillatory states. Thus, minor
371 modifications in the properties of I_{SA} enabled distinct functions in individual cells that otherwise belong
372 to the same neuronal class.

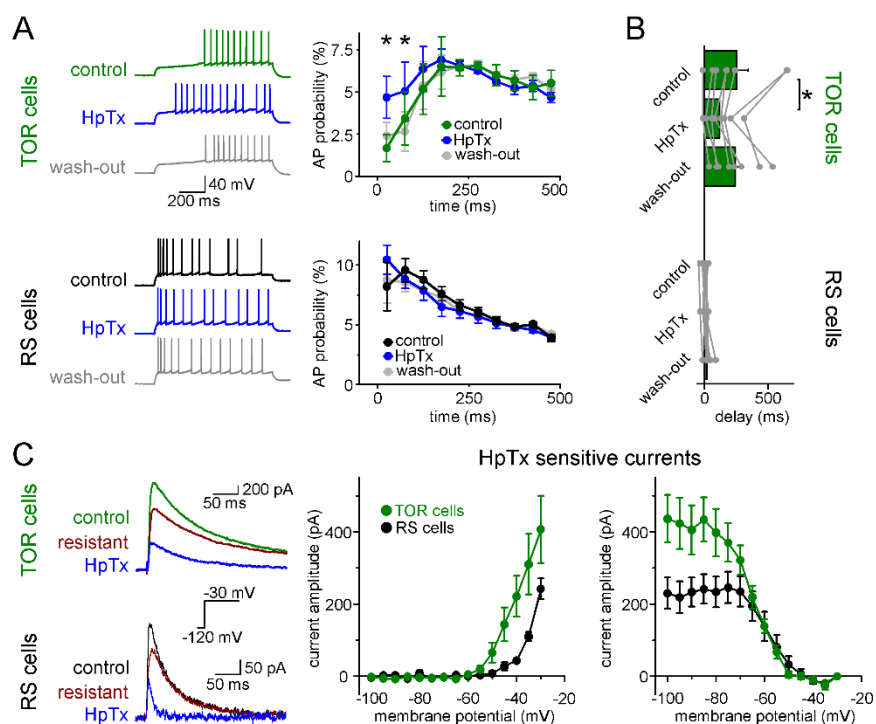
373

374 **Kv4 channels are responsible for both types of I_{SA} currents in CCK+INs**

375 Next, we investigated the identity of potassium channel subunits responsible for the differences of I_{SA} in
376 RS and TOR cells and for the MP-dependent firing in TOR cells. Neither TEA (0.5 and 10 mM, blocking
377 Kv3 channels) nor low concentration of 4-AP (100 μ M, blocking Kv1 and Kv3 channels) eliminated the
378 initial firing gap in TOR cells ([Figure 5 – figure supplement 1](#)). Only a high concentration of 4-AP (5
379 mM) was able to diminish the TOR phenomenon in CCK+INs. These results, together with the low voltage
380 activation properties, suggest a key role for Kv4 channels (Lien et al., 2002). Kv4.3 has been shown in
381 hippocampal CCK+INs (Bourdeau et al., 2007, Kollo et al., 2006). To specifically test the contribution of
382 Kv4 channels to the TOR phenomenon, we applied Heteropodatoxin-1 (HpTX, 1 μ M), which selectively,
383 but only partially, blocks Kv4.2 and Kv4.3 subunit-containing channels (DeSimone et al., 2011,
384 Sanguinetti et al., 1997). In the presence of HpTX, significantly more APs were evoked in TOR cells
385 during the first 125 ms of the stimulus compared to control conditions in the same cells before HpTX
386 application ([Figure 5A](#), from -80 mV preceding MP, $9.7 \pm 2.9\%$ vs $5.1 \pm 2.2\%$, respectively, $p=0.0037$,
387 $t(5)=-5.12$, *paired t-test*). Furthermore, the delay of the first APs was reversibly shortened from 239 ± 61
388 ms to 116 ± 38 ms ([Figure 5B](#), $p = 0.01$, $t(7)=3.493$, *paired t-test*, $n = 8$ TOR cells). However, HpTX did
389 not change the number and temporal distribution of APs in TOR cells from -60 mV (data not shown), nor
390 the firing of RS cells neither at -80 nor -60 mV. HpTX did not influence the half-width of the APs (TOR

391 cells: control: 0.48 ± 0.02 ms, HpTX: 0.52 ± 0.03 ms, $p = 0.15385$, $t(7) = -1.59901$, $n = 8$; RS cells:
 392 control: 0.55 ± 0.04 ms HpTX: 0.59 ± 0.06 ms, $p = 0.11016$, $t(7) = -1.82865$, $n = 8$). Thus, HpTX-
 393 sensitive, Kv4-mediated currents are crucial for the TOR phenomenon.

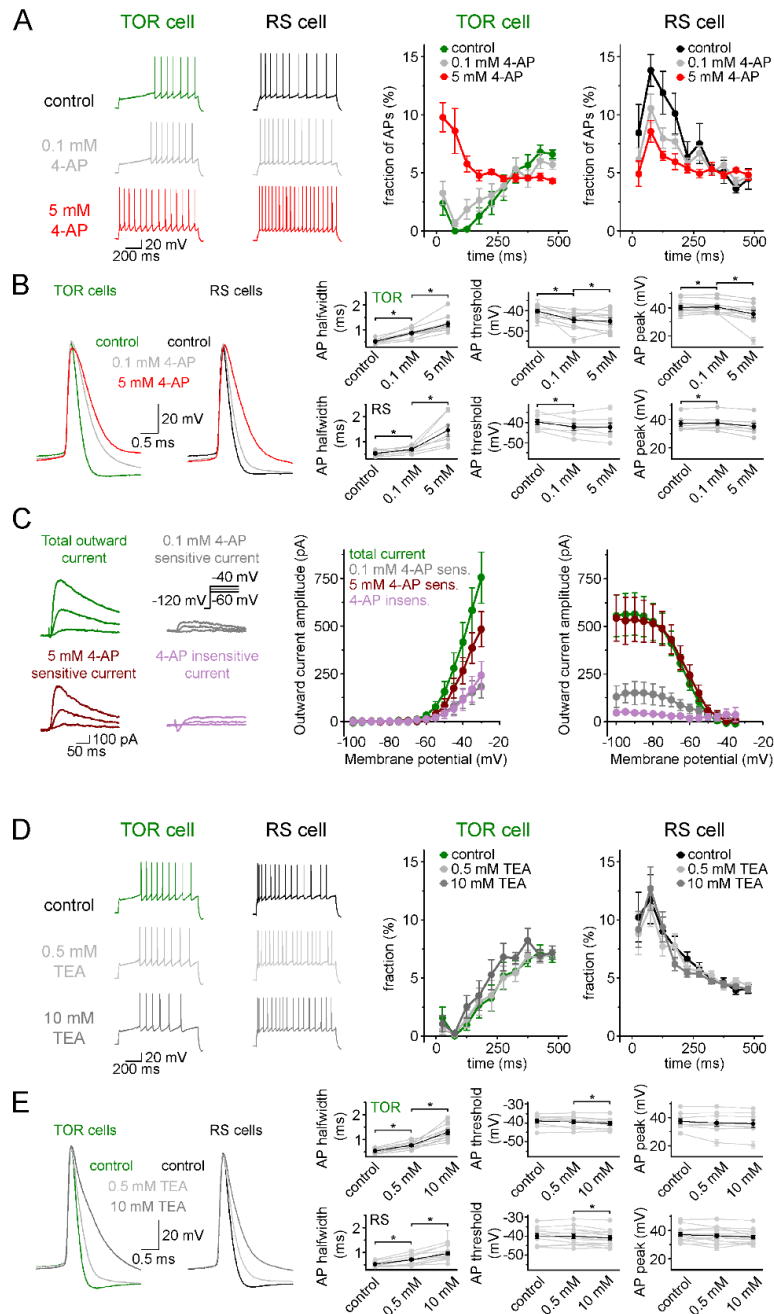
394 Next, we analyzed the contribution of HpTX-sensitive currents to I_{SA} in TOR and RS cells. Both types
 395 had substantial amounts of HpTX-sensitive currents. However, their properties were different in TOR and
 396 RS cells similarly as seen for their total I_{SA} . In TOR cells, the HpTX-sensitive current activated at more
 397 negative voltage than in RS cells (Figure 5C). The time constant of inactivation of the HpTX-sensitive
 398 currents was slower in TOR cells than in RS cells (49.1 ± 12.6 ms, and 11.8 ± 1.6 ms, respectively, at -25
 399 mV). The voltage dependence of inactivation of the HpTX-sensitive current was also left-shifted in TOR
 400 relative to RS cells ($V_{1/2}$ TOR: -64.0 ± 0.6 mV, RS: -56.8 ± 1.3 mV). Considering the similar kinetics and
 401 voltage dependence of total and HpTX-sensitive I_{SA} currents and the partial Kv4-blocking ability of HpTX
 402 (DeSimone et al., 2011, Sanguinetti et al., 1997), these results suggest that the majority of inactivating I_{SA}
 403 potassium currents in both types of CCK+INs are mediated by Kv4 channels.



404

405 **Figure 5. Blockade of Kv4 channels selectively inhibits TOR phenomenon.**

406 **A.** Representative CCK+INs firing patterns recorded before, during and after HpTx application (in response to
 407 identical current steps) and the average AP probabilities in TOR ($n = 6$) and RS cells ($n = 9$) from hyperpolarized
 408 MP ranges (-82 to -77 mV). **B.** Average delay of the first AP and reversible effect of HpTx. Connected symbols
 409 represent individual measurements (*paired t-test*: $p = 0.01008$). **C.** HpTx-sensitive I_{SA} in representative TOR and
 410 RS cells (left) and the average voltage dependence ($n = 7$ for both TOR and RS cells).



411

412 **Figure 5- figure supplement 1. TOR phenomenon is not affected when Kv1 and Kv3 channels are inhibited.**

413 **A.** Inhibition of spiking in TOR cells was eliminated by only a high concentration of 4-aminopyridine (4-AP, 5
 414 mM, red traces), but not by low concentration (0.1 mM, grey traces). **B.** As expected, both low and high
 415 concentrations of 4-AP affect AP width and threshold due to blockade of various potassium channels (grey symbols
 416 represent individual experiments, black symbols show average results). **C.** Representative traces on the left show
 417 control and 4-AP-sensitive and insensitive currents from a TOR cell and the graphs show the average voltage
 418 dependence of these components (n = 5 TOR cells). Majority (64.2% at -30 mV) of outward currents in TOR cells
 419 are sensitive to high, but not to low concentration 4-AP. **D.** Firing patterns of TOR and RS cells are not affected by
 420 low (0.5 mM, light grey) and high concentrations (10 mM, dark grey) of tetraethylammonium (TEA, n = 9 TOR
 421 and n = 13 RS cells). **E.** The effect of TEA on AP shape of TOR and RS cells (*: p < 0.05, paired sample t-test).

422

423 Next, we tested the presence of Kv4 channels in RS and TOR cells using the above SC-RNAseq data
424 ([Figure 6A-B](#)). Kv4.2 was absent in most of the tested 17 CCK+INs confirming previous findings
425 (Bourdeau et al., 2007, Rhodes et al., 2004). The mRNA of Kv4.3 subunits was detected in most CCK+INs
426 (16 out of 17 cells), including both RS and TOR types, in agreement with the findings that both RS and
427 TOR cells have HpTX-sensitive currents. Interestingly, in line with the predictions of the simulation, the
428 average RNA copy number of Kv4.3 was slightly higher in the tested RS cells compared to TOR cells.
429 Note that the SC-RNAseq data revealed differences in additional Kv channels between RS and TOR cells
430 such as Kv3.2, Kv1.3 and Kv1.6 subunits ([Figure 6A](#)). Because these subunits do not generate low-
431 voltage-activated, inactivating currents, we did not perform experiments to investigate the currents
432 generated by these subunits (Lien et al., 2002 , [Figure 5 – figure supplement 1](#)). We next performed
433 immunohistochemistry to localize Kv4.3 subunits in biocytin-filled TOR and RS cells. In general, we
434 observed an intense neuropil labelling for Kv4.3 in DG, CA3 strata radiatum and oriens, but not in the
435 CA1 area. A subset of INs were also labelled throughout the hippocampus (Bourdeau et al., 2007, Rhodes
436 et al., 2004). Kv4.3 proteins appeared to be enriched in the somatic and dendritic plasma membranes, but
437 the subcellular distribution was often uneven and clustered ([Figure 6D](#) and [Figure 6 – figure supplement](#)
438 [1A](#)) in line with the known distribution pattern of the Kv4.3 subunit (Kollo et al., 2006). In agreement
439 with the pharmacological and SC-RNAseq, data we detected Kv4.3 proteins ([Figure 6B, C](#)) in both TOR
440 (15 out of 20 tested cells) and RS CCK+INs (19 out of 23 cells). However, the immunosignal for Kv4.3
441 was usually stronger in RS than in TOR cells even within the same sections. This tendency was also seen
442 in the CA3 area obtained from perfusion-fixed brain ([Figure 6 – figure supplement 1A](#)), where Kv4.3
443 signal was detectable at strong or moderate level in most CCK/Satb1- cells (putative RS cells, 99%, 338
444 out of 342 tested cells), whereas the labelling was weak or hardly detectable in most CCK/Satb1+ cells
445 (putative TOR cells, 97%, 78 out of 80 tested cells). TOR and RS cells not only possess Kv4.3-mediated
446 I_{SA} with different activation and inactivation kinetics, but TOR cells seem to achieve larger charge transfer
447 via lower density of Kv4.3 channels. What could mediate such differences?

448

449 **Auxiliary subunits of Kv channels in TOR and RS cells**

450 Core Kv4 channel proteins form ternary complexes with dipeptidyl aminopeptidase-like proteins (DPLPs,
451 including DPP6 or DPP10) and K⁺ channel interacting proteins (KChIP1-4 from Kcni1-4 genes), which
452 fundamentally change the current properties. The modulatory effects are highly variable and depend on
453 the type and splice isoforms of the available auxiliary subunit. For example, most KChIP isoforms enhance

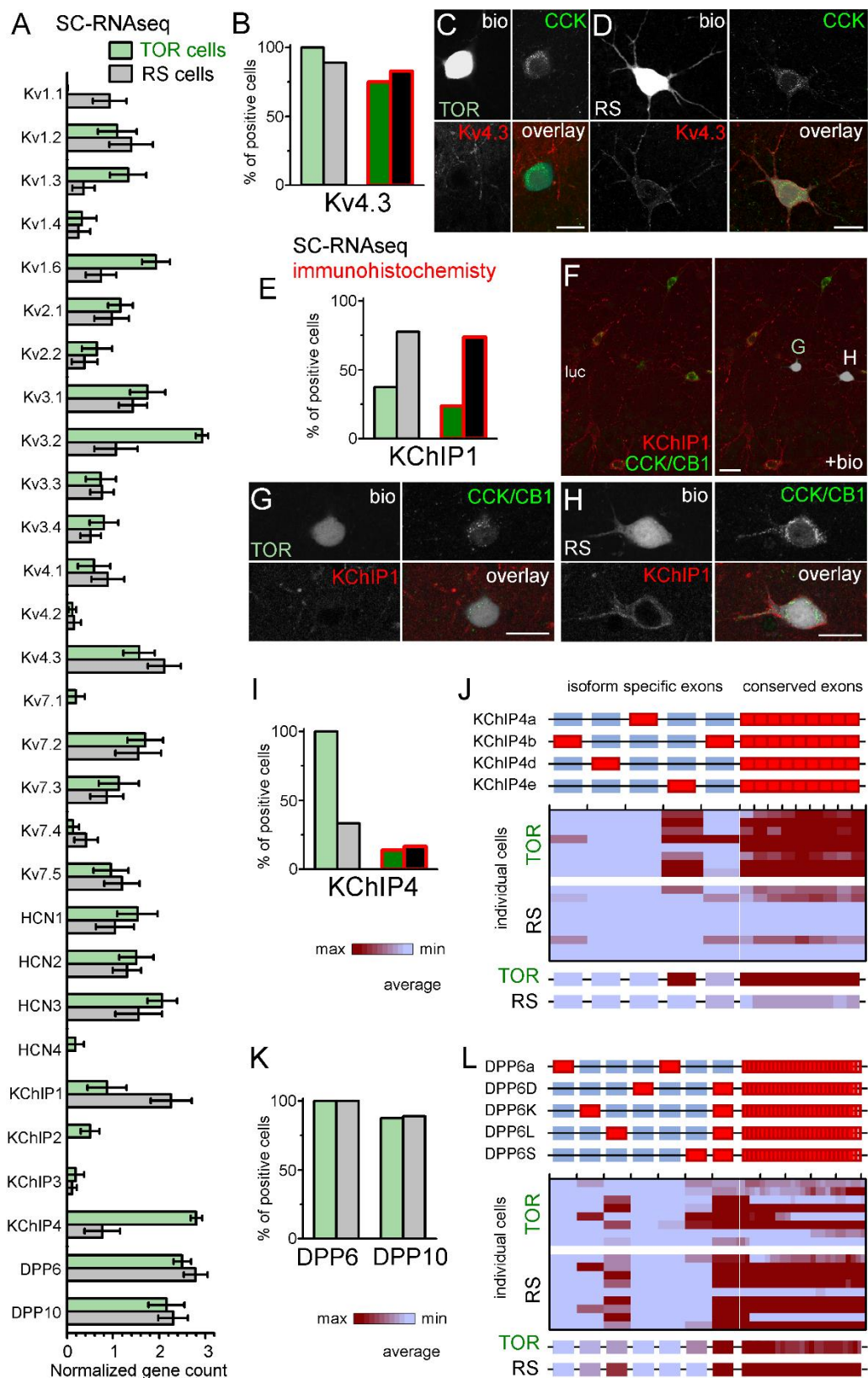
454 surface expression and accelerate inactivation and recovery from inactivation (Jerng and Pfaffinger, 2014,
455 Pongs and Schwarz, 2010). However, the so-called transmembrane KChIPs (tmKChIPs) have opposite
456 effects as they can retain Kv4 from the plasmamembrane and decelerate inactivation (Holmqvist et al.,
457 2002, Jerng and Pfaffinger, 2008, Jerng and Pfaffinger, 2014, Pruunsild and Timmusk, 2012).

458 KChIP1, as one of the classical KChIPs, accelerates inactivation and increases surface expression of Kv4.3
459 channels (Beck et al., 2002, Bourdeau et al., 2011, Jerng and Pfaffinger, 2014, Pongs and Schwarz, 2010).
460 We detected KChIP1 mRNA in most RS cells (7 of 9 tested), but it was absent in 5 out of 8 TOR. The
461 average mRNA level was significantly higher in RS than in TOR cells (2.26 ± 0.44 , TOR: 0.87 ± 0.42 ,
462 Mann-Whitney, $p = 0.013$, $z = -2.475$). Detection of the KChIP1 protein by immunohistochemistry
463 revealed an even clearer distinction between RS and TOR cells ([Figure 6E](#)). The KChIP1 protein was
464 detected in the majority of tested RS cells (20 out of 27), whereas only few TOR cells showed positive
465 immunoreaction (5 out of 21) and the signal in these cells was weaker than in RS cells ([Figure 6F-H](#)).
466 KChIP1 signal was present not only in the plasma membrane but also in the cytosol, in agreement with
467 their trafficking role (Pongs and Schwarz, 2010). This data from recorded cells were confirmed by the
468 analysis of CCK+INs in perfusion fixed brains ([Figure 6 - figure supplement 1A](#)). We detected strong
469 KChIP1 signal in the majority of CCK+/Satb1- cells (corresponding to RS cells, 122 out of 132 tested
470 cells, 92.4%). In contrast, only 4.9% of CCK+/Satb1+ cells (corresponding to TOR cells, 2 out of 41 tested
471 cells) showed strong KChIP1 immunosignal. We did not detect significant amounts of KChIP2 and
472 KChIP3 mRNAs in CCK+INs.

473 The universal mRNA sequence of KChIP4s was detected in all TOR cells (8 out of 8), whereas it occurred
474 in 3 out of 9 RS cells. The available antibody detected KChIP4 protein only in a very few CCK+INs
475 regardless of their firing type (4 out of 29 TOR, 5 out of 30 RS cells, [Figure 6I](#) and [Figure 6 – figure](#)
476 [supplement 1B-E](#)), thus, our observation with immunohistochemistry apparently contradicts the mRNA
477 data. In general, the relatively weak KChIP4 immunosignal in CCK+INs was surrounded by strong
478 neuropil labelling in the stratum radiatum ([Figure 6 - figure supplement 1B](#)). While KChIP1 is expressed
479 only in INs, KChIP4 is known to be associated with Kv4.2 channels in pyramidal cells as well (Rhodes et
480 al., 2004). This is in accordance with our observation of KChIP4 immunosignal at high magnification
481 ([Figure 6 - figure supplement 1D](#)), where it appears associated with tube-like structures, likely
482 representing the plasma membranes of putative pyramidal cell dendrites. However, our KChIP4-specific
483 antibody was raised against a long amino acid segment, which includes the highly variable N-terminal
484 region, which endow the various KChIP4-isoforms with different effects on Kv4 channel function
485 (Holmqvist et al., 2002, Jerng and Pfaffinger, 2008, Jerng and Pfaffinger, 2014, Pruunsild and Timmusk,

486 2012). Therefore, we further analyzed the mRNA data at the level of individual KChIP4 exons ([Figure](#)
487 [6J](#)). We detected the KChIP4e isoform-specific exon in 7 TOR cells (out of 8 tested). KChIP4e belongs
488 to the so-called transmembrane KChIPs (tmKChIPs) (Jerng and Pfaffinger, 2008), which, in contrast to
489 most KChIP types and isoforms, do not promote the plasma membrane expression of Kv4 and have
490 opposite effects on the inactivation kinetics (Jerng and Pfaffinger, 2008, Pruunsild and Timmusk, 2012).
491 KChIP4b, which acts as classical KChIPs, was detected in only one TOR cell (from 8 tested). KChIP4e
492 specific exons were detected only in one RS cell. The two other RS cells that also had a small amount of
493 KChIP4, expressed the KChIP4b isoform. Altogether, these data indicate that RS cells express KChIP1,
494 whereas TOR cells primarily express KChIP4e. We suggest that the differential influences of these
495 auxiliary subunits underlie some of the distinct properties of I_{SA} in RS and TOR cells because KChIP1 is
496 known to accelerate inactivation and increase surface expression, whereas tmKChIPs, such as KChIP4e,
497 do not facilitate Kv4 plasma membrane trafficking and confer slow channel inactivation.

498 KChIPs alone do not account for all differences between I_{SA} currents in TOR and RS cells, including
499 differences in voltage-dependence. DPP10 and DPP6 proteins effectively shift the voltage dependence of
500 Kv channel activation and inactivation (Jerng et al., 2007, Jerng and Pfaffinger, 2012, Jerng and
501 Pfaffinger, 2014, Nadal et al., 2006, Nadal et al., 2003, Pongs and Schwarz, 2010). Therefore, next we
502 analyzed the expression of these molecules at the mRNA level ([Figure 6K-L](#)). DPP10 (conserved
503 segments) was present in both TOR and RS cells (7 out of 8, and 8 out of 9 cells, respectively). The
504 DPP10c isoform was detected in significant amounts in all cells regardless of their firing type. DPP6 was
505 also detected in most CCK+INs from both types. The primary isoform in RS cells was the DPP6L. In
506 contrast, DPP6S isoform occurred in most TOR cells (7 out of 8 cells) and DPP6L-specific exons were
507 also detected in several cells (4 out of 8 TOR cells). Thus, in addition to KChIPs, expression of DPLP-
508 isoforms correlates with the firing types of CCK+INs and their combined modulatory effects may underlie
509 the different properties of Kv4.3-mediated I_{SA} currents, which is responsible for their different excitability.



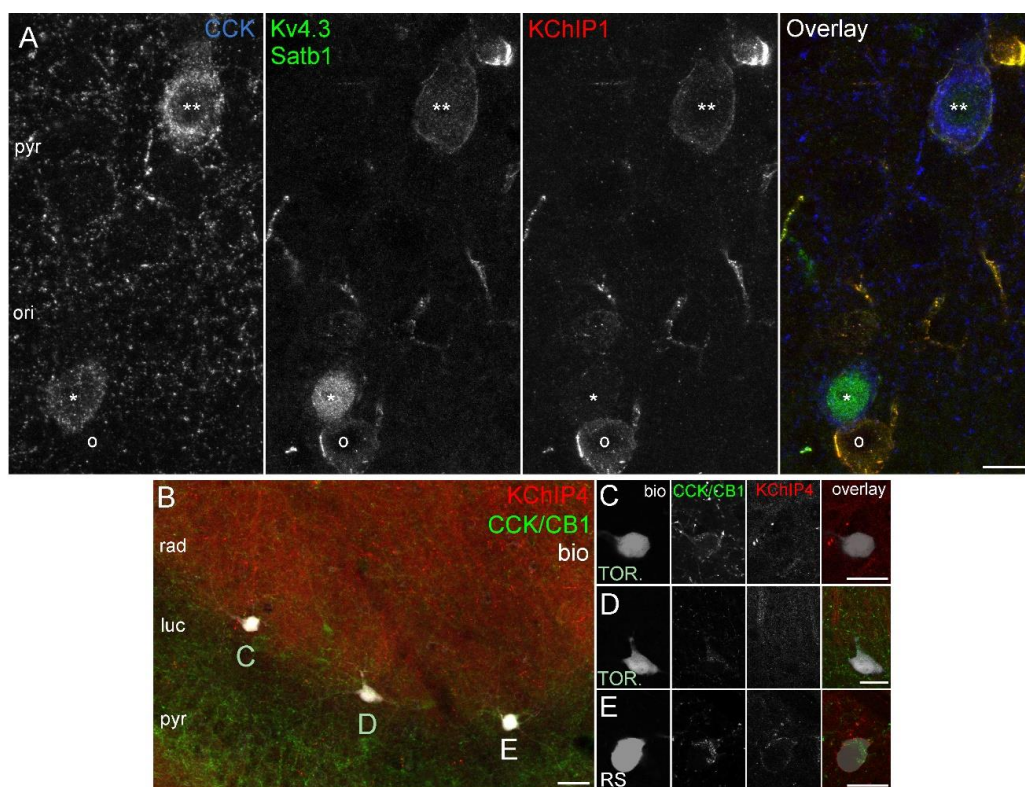
510

511 **Figure 6. Similar Kv4.3-expression and different auxiliary subunit, KChIP and DPP-content in CCK+INs.**

512 **A.** Normalized gene count of primary and auxiliary subunits of voltage-gated potassium channels from single cell

513 **RNAseq** data of TOR (n = 8) and RS (n = 9) cells. **B.** Percentage of recorded cells with detectable levels of Kv4.3

514 mRNA (left bars, n = 8 and 9 cells) and protein (right bars, n = 20 and 23 tested cells). **C-D**. Immunofluorescent
 515 co-localization of CCK and Kv4.3 in a TOR (**C**), and a RS cell (**D**) in CA3 stratum lucidum. **E**. Percentage of
 516 recorded cells with detectable levels of KChIP1 mRNA (n = 8 and 9 cells) and proteins (n = 20 and 27 cells). **F-H**.
 517 Immunofluorescent co-localization of CCK with CB1 (green) and KChIP1 in a TOR (**G**), and a RS cell (**H**) from
 518 the same slice shown in low magnification image (**F**). **I**. Percentage of recorded cells with detectable levels of
 519 KChIP4 mRNA (left bars, n = 8 and 9 cells) and protein (right bars, n = 29 and 30 tested cells). **J**. Major KChIP4
 520 splicing isoforms consist of different exons in the N-terminal region (represented as red boxes). Each row represents
 521 a single cell in the color-mapped data and columns correspond to individual exons aligned to the schematic
 522 illustration of isoforms above. Red and blue colors code high and low mRNA levels, respectively. The average exon
 523 counts from the two types of CCK+INs (n = 8 and 9) are shown at the bottom using the same color code scheme.
 524 **K**. Percentage of recorded cells with detectable levels of DDP6 and DPP10 mRNA. **L**. Assembly of major DPP6
 525 isoforms and exon levels in individual CCK+INs are shown as above (J).
 526



527
 528 **Figure 6 – figure supplement 1. Kv4.3 and KChIP immunohistochemistry in perfusion or immersion fixed**
 529 **CA3 slices.**
 530 **A.** CCK+ cells in CA3 obtained from perfusion fixed brain. One CCK+ cell (***) is outlined by intense Kv4.3 and
 531 KChIP1 immunolabelling. In the other CCK+ cell (*) that is strongly labelled for Satb1 in the nucleus, the Kv4.3
 532 and KChIP1 signals are only weakly detectable, whereas they both intensely decorate a neighbouring CCK-negative
 533 neuron (o). **B.** Low magnification image showing simultaneous immunolabelling of KChIP4 (red) and CCK/CB1
 534 (green) in an acute CA3 slice, in which a RS cell and two TOR cells were filled with biocytin (left) at the border of
 535 strata radiatum/lucidum in CA3a. Intense KChIP4 immunolabelling is present in the neuropil of stratum radiatum
 536 mainly associated with dendrites of pyramidal cells (Rhodes et al., 2004). **C-E.** High magnification images showing
 537 an enlarged view of the biocytin filled cells shown in (**B**). KChIP4 is not detectable in the two TOR cells (**C**, **D**),
 538 but its weak presence was detected in the neighbouring the RS cell (**E**), but. Scale bars: 10 μ m (**A**) 20 μ m (**B-E**).

539 Discussion

540 CCK+INs can dynamically select cell assemblies and control their activity during theta oscillations, which
541 dominate hippocampal operation during spatial navigation and memory tasks (Klausberger and Somogyi,
542 2008). Therefore, it is particularly important that the excitability of TOR and RS cells are drastically
543 different when they are excited within 8-15 Hz input range. This suggests that under basal conditions it is
544 unlikely that TOR cells can substantially contribute to theta oscillations unless they are primed by
545 preceding depolarizations. By contrast, TOR and RS cells may play similar roles during lower and faster
546 network oscillations. Thus, because distinct network state-dependent contribution is considered as a cell
547 type classification criteria (Klausberger and Somogyi, 2008), TOR and RS cells can be viewed as separate
548 partitions within the CCK+IN class. Furthermore, the TOR phenomenon can also contribute to the variable
549 recruitment of individual CCK+INs during subsequent theta cycles (Freund and Katona, 2007,
550 Klausberger et al., 2005).

551 Despite the functional distinction between TOR and RS cells, their morphology, basic
552 electrophysiological characteristics and most genes are surprisingly similar. One notable difference is the
553 presence of transcription regulator *Satb1* in most TOR cells and absence in most RS cells. However, we
554 did not detect systematic differences in the complete transcriptome of TOR and RS cells. Even those genes
555 and proteins were present in both types similarly that have been shown previously to delineate certain
556 subpopulations within CCK+INs (such as *VGluT3* or *Calb1*). Thus, TOR and RS cells cannot be
557 distinguished based on their general gene expression profiles, which is recently used for identification of
558 individual cell types (Fuzik et al., 2016, Harris et al., 2018). Furthermore, the morphology of RS and TOR
559 cells covers the same diversity including soma and dendrite targeting axons and we did not recognize
560 differences in their AP shape and synaptic inputs. Thus, it is difficult to determine whether TOR and RS
561 CCK+INs comply with conventional definitions of cell types in spite of their potential different
562 contributions to network operations.

563
564 **Same channel protein but distinct auxiliary subunits are responsible for the different I_{SA} currents**
565 **and for the different functionality of TOR and RS cells**

566 Our simulations showed that $Kv4.3$ current alone is sufficient for the oscillation frequency-dependent
567 functionality among CCK+INs because changing only I_{SARS} to $I_{SATOR+RS}$ in the same realistically
568 modelled CCK+INs specifically silenced them during 8-15 Hz input regimes and reproduced the recorded
569 differences in their firing. The recordings confirmed the crucial role of $Kv4.3$ channels in TOR firing.

570 However, RS cells also express Kv4.3 channels, and in fact, their density is higher in RS cells compared
571 to TOR cells. Thus, paradoxically, in spite of Kv4.3 mediated currents are responsible for the unique and
572 distinctive firing properties of TOR cells, Kv4.3 currents are present in both cell firing types. We found
573 the potential explanation that solves this paradox in differences of the auxiliary subunits that can modify
574 the function of Kv4.3 channels.

575 KChIP1 is strongly expressed by RS cells, whereas most TOR cells lacked this cytosolic auxiliary subunit.
576 The known effects of the KChIP1 (Beck et al., 2002, Bourdeau et al., 2011, Jerng and Pfaffinger, 2014,
577 Pongs and Schwarz, 2010) correlate well with the properties of the I_{SA} in RS cells. As a classical KChIP,
578 KChIP1 increases surface expression of Kv4 channel complex. Indeed, we measured larger density of I_{SA}
579 current in outside out patch from RS cells than in TOR cells. We also observed that Kv4.3 immunosignal
580 was usually stronger in RS cells than in TOR cells. Furthermore, we were able to reproduce TOR and RS
581 firing phenotypes in the realistically simulated conditions only if the total amount of I_{SA} conductance was
582 larger in RS cells than in TOR cells. The apparent paradox between larger current density and the smaller
583 measured current amplitude near the AP threshold in RS cells derives from the differences in the voltage
584 dependence of activation of I_{SA} in RS and TOR cells. I_{SA} channels are submaximally activated at
585 physiological subthreshold voltage. However, because of the left-shifted activation curve, a much larger
586 fraction of I_{SA} channels are activated in TOR cells at lower voltage ranges. Therefore, larger currents can
587 be generated even by a smaller number of channels. Another substantial influence of KChIP1 on Kv4.3 is
588 the acceleration of steady-state inactivation kinetics and the recovery time from inactivation (Beck et al.,
589 2002, Bourdeau et al., 2011, Jerng and Pfaffinger, 2014, Pongs and Schwarz, 2010). These are also
590 correlated well with the differences of I_{SA} in RS and TOR cells, as both parameters were much faster in
591 the former type of cells.

592 KChIP4 was the dominant KChIP in TOR cells and it was not detected in most RS cells. Our data also
593 showed that TOR cells expressed a special splicing isoform, KChIP4e, which belongs to the so-called
594 tmKChIPs (Holmqvist et al., 2002, Jerng and Pfaffinger, 2008, Jerng and Pfaffinger, 2014, Pongs and
595 Schwarz, 2010). In contrast to classical KChIPs, all tmKChIPs including KChIP4e do not facilitate surface
596 expression of Kv4 channels (Holmqvist et al., 2002, Jerng and Pfaffinger, 2008, Pruunsild and Timmusk,
597 2012). As explained above, several lines of evidence suggest lower Kv4.3 channel density in the KChIP4e-
598 expressing TOR compared to KChIP1-expressing RS cells. The presence of tmKChIPs results in slow
599 inactivation kinetics, often slower than that of the solitary Kv4 channels (Holmqvist et al., 2002, Jerng et
600 al., 2007, Jerng and Pfaffinger, 2008, Tang et al., 2014). As a consequence of enhanced closed-state
601 inactivation of Kv4.3 channels, KChIP4a causes a leftward shift in the voltage dependence of inactivation

602 (Tang et al., 2013, Tang et al., 2014). Albeit it is a likely possibility due to the similarity of their N-terminal
603 domains, it remains to be answered whether the effects of KChIP4e on Kv4.3 kinetics are similar to the
604 other studied tmKChIPs. The slower inactivation and recovery of I_{SA} in KChIP4e-expressing TOR cells
605 were critical for their unique functionality during 8-15 Hz network states because they define the
606 availability of the I_{SA} conductance. KChIP4 was present only in three RS cells and two of them expressed
607 the KChIP4b isoform, which is a classical KChIP that, similarly to KChIP1s results in much faster
608 inactivation and recovery (Jerng and Pfaffinger, 2008). We should also note that the apparent discrepancy
609 in KChIP4 detection between the mRNA and protein levels may also be explained by the presence of
610 different isoforms, as our antibody may have targeted the highly variable N-terminal region.

611 Both DPLPs were present in TOR and RS cells. DPP10c isoform, which is known to affect voltage
612 dependence of Kv4 channels, but does not accelerate inactivation (Jerng et al., 2007), was ubiquitous in
613 both types of CCK+INs. Albeit all tested CCK+INs had a significant amount of DPP6 mRNA, TOR and
614 RS cells expressed different isoforms. RS cells expressed only DPP6L and in TOR cells the primary
615 isoform was DPP6S (but DPP6L was also present in several cells). DPP6S can contribute to the left-
616 shifted voltage dependence of activation of I_{SA} in TOR cells. The left-shifted voltage dependence is
617 important for the sufficient prevention of spiking. The dual set of DPP6 proteins fits well with our
618 observations that many properties of TOR cells can be described only if two populations of Kv4.3-
619 mediated currents are present. Altogether, these observations suggest that apparently small modifications
620 in the available components of ion channel complexes underlie the different functions of TOR and RS
621 cells.

622 The net effects of KChIPs and DPLPS are not simply the sum of the effects of individual subunits. Some
623 subunits either dominate others or the interaction can result in unique combinations of effects (Jerng et
624 al., 2005, Nadal et al., 2006, Zhou et al., 2015). For example, when DPP6K is present, KChIP4e causes a
625 leftward shift of the voltage dependence of inactivation and deceleration of the recovery from inactivation
626 compared to other KChIPs (Jerng and Pfaffinger, 2012). In this regard, it is an important observation for
627 our results that DPP6S, unlike some other DPLPs, cannot overcome the tmKChIP4-mediated deceleration
628 of inactivation (Jerng et al., 2007, Jerng and Pfaffinger, 2008, Seikel and Trimmer, 2009). Thus, the
629 expression of DPP6S in TOR cells may preserve the unique modulatory effects of KChIP4e. Because of
630 the composition of these ternary channel complexes by multiple proteins and splicing variants, whose
631 interactions are not yet characterized, the exact contribution of individual components of
632 DPP6S/L/DPP10c-KChIP4e-Kv4.3- and DPP6L/DPP10c-KChIP1-Kv4.3-complexes cannot be predicted
633 yet. Nevertheless, the higher channel density, faster inactivation kinetics and faster recovery from

634 inactivation of I_{SA} in RS compared to TOR cells are consistent with the differential expression of KChIP1
635 and KChIP4e, and the cell type-specific expression and contributions of DPP10c, DPP6L and DPP6S are
636 expected to explain unique voltage-dependency in the two types of CCK+INs without the involvement of
637 additional differences between RS and TOR cells. Thus, the different firing properties and responsiveness
638 during 8-15 Hz network states of RS and TOR cells are established by surprisingly minor modifications
639 in a few auxiliary subunits.

640

641 **Methods**

642 Animal protocols and husbandry practices were approved by the Institute of Experimental Medicine Protection
643 of Research Subjects Committee (MÁB-7/2016 for slice recording and anatomy experiments and MÁB-2/2017
644 for immunolabelling experiments in perfusion fixed brains). by the Veterinary Office of Zurich Kanton
645 (ZH241/15, single cell RNAseq experiments).

646

647 **Slice preparation, solutions and chemicals** Hippocampal slices were prepared from 21-33 days old Wistar rats
648 (deeply anaesthetized with isoflurane) in ice-cold artificial cerebrospinal fluid (85 mM NaCl, 75 mM sucrose,
649 2.5 mM KCl, 25 mM glucose, 1.25 mM NaH_2PO_4 , 4 mM MgCl_2 , 0.5 mM CaCl_2 , and 24 mM NaHCO_3 , Leica
650 VT1200 vibratome). The slices were incubated at 32 °C for 60 minutes after sectioning and were then stored at
651 room temperature until they were used. The normal recording solution was composed of 126 mM NaCl, 2.5 mM
652 KCl, 26 mM NaHCO_3 , 2 mM CaCl_2 , 2 mM MgCl_2 , 1.25 mM NaH_2PO_4 , and 10 mM glucose. For standard
653 recordings, pipettes were filled with an intracellular solution containing 90mM K-gluconate, 43.5 mM KCl, 1.8
654 mM NaCl, 1.7 mM MgCl_2 , 0.05 mM EGTA, 10 mM HEPES, 2 mM Mg-ATP, 0.4 mM Na_2 -GTP, 10 mM
655 phosphocreatine, and 8 mM biocytin (pH 7.2; 270–290 mOsm). Chemicals for the intra- and extracellular
656 solutions were purchased from Sigma-Aldrich, ion channel blockers were from Tocris or Alomone and
657 fluorophores were from Invitrogen.

658 **Somatic recordings** For recordings, cells in slices were visualized with an upright microscope (Eclipse FN-1;
659 Nikon) with infrared (900 nm) Nomarski DIC optics (Nikon 40x NIR Apo N2 NA0.8W objective).
660 Electrophysiological recordings were performed at 34.5-36°C. During current-clamp recordings, firing patterns
661 were elicited by square shaped current pulses with increasing amplitudes (starting from -100 pA up to 700 pA,
662 $\Delta 20$ pA, duration: 1 sec) or with standard steps (eliciting average firing between 10-20 Hz), which was preceded
663 by 3-second-long different amplitude holding current steps () to reach preceding MP range between -90 and -
664 50 mV. The action potential (AP) distributions were calculated from all recorded traces, which contained action
665 potentials and binned by 50 ms from each recorded cell. In these recordings, the pipette capacitance was

666 neutralized (2.5-5 pF remaining capacitance) and bridge balance compensation was set to eliminate apparent
667 voltage offsets upon current steps. Voltage values were not corrected for the liquid junction potential
668 (theoretically: -15.4mV). Traces were low pass filtered at 6–20 kHz and digitized at 40–100 kHz using a
669 Digidata 1440 A interface (Molecular Devices).

670 For voltage-clamp recordings, cells were patched in normal extracellular solution to first record their firing
671 patterns, and then 2.5 μ M TTX and 10 μ M ZD7288 was added to block sodium and I_h currents respectively.
672 Voltage protocols for potassium current measurements consisted of a 300 ms long conditioning pulse at -120 mV,
673 followed by a 300 ms long voltage steps between -120 and -20 mV (for current activation and decay time constant
674 measurements), and a last voltage step to -30 mV for 100 ms (to measure voltage dependence of potassium current
675 inactivation). Series resistances were between 6-20 M Ω (75-80% compensated with 53 μ s lag) and were constantly
676 monitored. Data were discarded if the series resistance changed more than 25%.

677 The recovery from inactivation test protocol consisted four voltage steps: (1) -120 mV for 345 ms, allowing full
678 recovery, (2) -30 mV for 500 ms, allowing complete inactivation, (3) -65, -75, -85 or -120 mV steps with variable
679 duration between 1-233 ms, (4) -30 mV test pulse, where area of current was analyzed according to the voltage and
680 duration of the preceding recovery step. Control traces (whose duration was identical to test pulses and steps 1 and
681 3 were set to -50 mV) were subtracted from each traces allowing the isolation of I_{SA} currents. Furthermore, these
682 measurements were performed in the presence of TTX, 1 mM 4-AP and 10 mM TEA to reduce contamination from
683 non-Kv4 channels.

684 **Outside-out patch recording** To obtain outside-out patch recordings, first we made somatic whole-cell
685 recordings from the selected cells using IR-DIC optics. This was necessary for classifying their firing as TOR
686 or RS cells, for loading biocytin for subsequent CCK immunolabelling, and for loading 20 μ M Alexa-594
687 fluorescent dye, which allowed the visualization of their dendrites. After at least a 5-minute-long loading period
688 the somatic pipette was retracted. Intact dendrites (30-80 μ m from the surface) were visualized and patched
689 using epifluorescent illumination (less than a minute illumination time). The thick-wall pipettes (resistance: 20-
690 55 M Ω) were filled with 5 μ M Alexa-594. After break-in, we confirmed that no neighboring structure was
691 loaded with the fluorescent dye and outside-out configuration was achieved by the slow retraction of the pipette.
692 By applying similar voltage steps as described for whole-cell voltage-clamp configurations, we recorded
693 dendritic potassium currents (without pharmacological isolation). After outside-out patch recordings, the pipette
694 was pushed into a Sylgard ball (Sylgard 184, Merck), and capacitive responses to voltage steps were recorded
695 and subtracted from the capacitive responses recorded in outside-out patch configuration. The surface area of
696 the patch membrane was calculated as described earlier (Gentet et al., 2000) with the specific membrane
697 capacitance determined from 18 nucleated patch experiments ($c_m = 1.015 \pm 0.014 \mu$ F/cm²). Distances of the
698 recording sites from the soma were measured based on posthoc epifluorescent or confocal images. Somatic
699 outside-out patches were obtained using the same protocol, with similar pipettes. Current traces were low pass

700 filtered at 10 kHz and digitized at 100 kHz. Capacitive membrane responses were digitized at 250 kHz, without
701 filtering. Leak and capacitive current components were subtracted during potassium current recordings using
702 online P/−4 method. Inactivating potassium currents (at 0 mV) were isolated offline by subtracting currents
703 obtained with a -50 mV prepulse from currents measured with a prepulse of -80 mV.

704 Anatomical and immunohistochemical characterization of CCK+ cells All recorded cells were filled with biocytin
705 and processed for immunohistochemistry. After the recordings, slices were fixed in 0.1 M phosphate buffer
706 containing 2% paraformaldehyde and 0.1% picric acid at 4 °C overnight. After fixation, slices were re-sectioned
707 at 60 μm thickness (Neubrandt et al., 2018). Immunopositivity for CCK was tested with a primary antibody
708 raised against cholecystokinin (1:1000, CCK, Sigma-Aldrich, Cat# C2581, RRID:AB_258806, rabbit
709 polyclonal). Biocytin labeling was visualized with either Alexa 350-, Alexa 488-, Alexa 594- or Alexa 647-
710 conjugated streptavidin. For additional neurochemical markers, further immunolabeling was used either against
711 Vesicular Glutamate Transporter 3 (1:2000, VGluT3; Merck, Cat#AB-5421, RRID:AB_2187832; guinea pig
712 polyclonal), Cannabinoid Receptor type 1 (1:1000, CB1R, Cayman Cat#10006590, RRID:AB_10098690, rabbit
713 polyclonal), special AT-rich sequence-binding protein-1 (1:400, Satb1; Santa-cruz Cat#sc-5989,
714 RRID:AB_2184337, goat polyclonal, 1:400), Reelin (1:400, Merck Cat#MAB5364, RRID:AB_2179313, mouse
715 monoclonal) or calbindin (1:1000, Calb1; Swant Cat#300, RRID:AB_10000347, mouse monoclonal). Only
716 those cells were included in the analysis, which were positive for CCK (or for CB1, n = 15 cells).

717 Known morphological subtypes of CCK+INs in the hippocampal CA3 region were determined based on the
718 layer-preference of their axonal arborization. Schaffer collateral associated cells (SCA)(Cope et al., 2002)
719 innervate dendrites in the stratum radiatum. Albeit the definition of basket cells (BCs) (Hendry and Jones, 1985)
720 and mossy-fiber associated cells (MFA) (Vida and Frotscher, 2000) are clear, with termination zones in the strata
721 pyramidale and lucidum, respectively, their practical identification is more complicated because both cell types
722 have a substantial amount of axons in the adjacent strata, especially near to their soma. Therefore, only cells with
723 extended axonal arbor (at least reaching 200 μm from soma) were identified either as BC or as MFA. In this
724 distal region, BCs had clearly targeted stratum pyramidale, whereas distal axons of MFA ran in the stratum
725 lucidum parallel with the cell layer, and they often invaded the hilar region of the dentate gyrus.

726 **Analysis of potassium channel subunits using immunohistochemistry** For perfusion fixed brain samples two
727 (P25 and P45) Wistar rats were anesthetized and perfused through the aorta with 4 % paraformaldehyde and 15
728 v/v% picric acid in 0.1M Na-phosphate buffer (PB, pH = 7.3) for 15 min. Immunohistochemistry was performed
729 on 70 μm thick free floating coronal sections from the hippocampus. We used a different fixation protocol for acute
730 hippocampal slices containing biocytin-filled cells. After short recordings (5-15 minutes), slices were transferred
731 to a fixative containing 2% paraformaldehyde and 15 v/v% picric acid in 0.1 M PB for 2 hours at room temperature.
732 Slices were washed in PB, embedded in agarose and re-sectioned to 70-100 μm thick sections. Sections were
733 blocked in 10% normal goat serum (NGS) in 0.5 M Tris buffered saline (TBS) for one hour and incubated in a

734 mixture of primary antibodies for one overnight at RT. The following antibodies were used: rabbit polyclonal anti-
735 CCK antibody (1:500, Sigma-Aldrich Cat# C2581, RRID:AB_258806) mixed either with a mouse monoclonal anti-
736 KChiP1 (1:500, IgG1, UC Davis/NIH NeuroMab Facility Cat# 75-003, RRID:AB_10673162), a mouse monoclonal
737 anti-KChiP4 (1:400, IgG2a, UC Davis/NIH NeuroMab Facility Cat# 75-406, RRID:AB_2493100), or a mouse
738 monoclonal anti-Kv4.3 antibody (1:500, IgG1, UC Davis/NIH NeuroMab Facility Cat# 75-017,
739 RRID:AB_2131966). In some sections, a rabbit polyclonal anti-CB1 receptor (1:2000, Cayman Chemical
740 Cat# 10006590, RRID:AB_10098690) was also used together with the CCK antibody to more reliably characterize
741 filled cells. Potential TOR cells were identified by Satb1 immunolabelling in the perfusion fixed sections. Satb1
742 and Kv4.3 were visualized by the same secondary antibody but their labelling pattern could be reliably distinguished
743 based on their different subcellular locations. The following secondary antibodies were used to visualize the
744 immunoreaction: Alexa 488-conjugated goat anti-rabbit (1:500, Thermo Fisher Scientific), Cy5 conjugated goat
745 anti-rabbit (1:500, Jackson ImmunoResearch), Alexa 488-conjugated goat anti-mouse IgG1 (1:500, Jackson
746 ImmunoResearch), and Cy3 conjugated goat anti-mouse IgG1 or IgG2a (1:500, Jackson ImmunoResearch) IgG-
747 subclass-specific secondary antibodies. Biocytin was visualized with Cy5 conjugated Streptavidin (1:1000, Jackson
748 ImmunoResearch). High magnification fluorescent images were acquired with an Olympus FV1000 confocal
749 microscope using a 60x objective (NA = 1.35).

750 **Single-cell mRNA** Single-cell mRNA was performed using the Clontech's SMARTer v4 Ultra Low Input RNA
751 Kit. Cells were collected via pipette aspiration into sample collection buffer, were spun briefly, and were snap
752 frozen on dry ice. Samples were stored at -80°C until further processing, which was performed according to the
753 manufacturer's protocol. Library preparation was performed using Nextera XT DNA Sample Preparation Kit
754 (Illumina) as described in the protocol. Then, cells were pooled and sequenced in an Illumina NextSeq500
755 instrument using 2×75 paired end reads on a NextSeq high-output kit (Illumina). After de-multiplexing the raw
756 reads to single-cell datasets, we used Trimmomatic and flexbar to remove short reads, remove adapter sequences
757 and trim poor reads. The remaining reads were aligned to the GRCm38 genome with STAR aligner. Aligned reads
758 were converted to gene count using RSeQC. All data analyses were performed using python3. The analysis included
759 the removal of poor quality cells (at least 3000 genes were detected in each cell), normalization of gene expression
760 data using scran, and analysis of differential expression of genes across cell types. Sequences of splicing variants
761 of KChiP4, DPP6, and DPP10 were validated in the NCBI Genebank and UCSC databases.

762 Genes related to apoptosis (Bcl2, Casp2, Casp8, Fas; not shown) were absent or present in low copy numbers in
763 both RS and TOR cells indicating that the two firing phenotypes are not due to differential damage during slice
764 preparation.

765 **Computational modelling** We performed computer simulations using the NEURON simulation environment
766 (version 7.5 and 7.6, downloaded from <http://neuron.yale.edu>). To create a realistic model of CCK+INs, first we
767 made detailed reconstructions of five biocytin labelled, electrophysiologically characterized cells (using

768 NeuroLucida and the Vaa3D software; Peng et al., 2010). The passive electrical parameters of the simulated cells
769 were set as follows: first, axial resistance values were set to $120 \Omega\text{cm}$, then specific membrane capacitance and leak
770 conductances (the substrate of membrane resistance) were fitted based on passive membrane responses to small
771 amplitude (20 pA) current injections (ranges: cm: $1.05 - 0.82 \mu\text{F}/\text{cm}^2$, gl: $5 \cdot 10^{-5} - 5.8 \cdot 10^{-5} \text{ S}/\text{cm}^2$). The set of active
772 conductances were selected based on a previous publication (Bezaire et al., 2016). The properties (voltage
773 dependence and kinetics) of these conductances were adjusted to reproduce firing characteristics representing our
774 average measurements (AP parameters: AP peak, AP half-width, AHP amplitude, AP threshold, and firing
775 parameters: accommodation of firing frequency, maximum AP frequency). Additionally, two variants of A-type
776 potassium conductance models were created. First, the ratio of somatic and dendritic inactivating potassium
777 conductances was set to 2.96:1 somatic to dendritic ratio (see [Figure 4- figure supplement 1](#)). Based on the
778 observation, that patches pulled from RS cells produced inactivating potassium currents with similar MP-
779 dependence to those recorded in whole-cell configuration, we modelled a single potassium conductance ($I_{\text{SA}^{\text{RS}}}$)
780 constrained on somatic whole-cell recordings (HpTx-1 sensitive currents measured in RS cells, [Figure 5C](#)), with
781 the appropriate uncompensated series resistance implemented in the models ($2.76 \pm 0.28 \text{ M}\Omega$, $n=14$). For TOR cell
782 models we used a mixture I_{SA} consisting of $I_{\text{SA}^{\text{RS}}}$ and $I_{\text{SA}^{\text{TOR}}}$, to account for the variability of patch currents from
783 TOR cells. $I_{\text{SA}^{\text{TOR}}}$ has a left shifted voltage dependence and slower inactivation than $I_{\text{SA}^{\text{RS}}}$. $I_{\text{SA}^{\text{TOR}}+\text{RS}}$
784 reproduced potassium currents from our whole-cell measurements and the typical characteristics of TOR firing.

785 To investigate the behavior of these model cells in *in vivo* relevant conditions constructed physiologically plausible
786 input conditions with a large number of temporally organized synaptic excitation and inhibition. For these, first we
787 measured the amplitude and kinetics of glutamaterg and GABAergic currents in TOR and RS cells, using intracellular
788 solutions, containing CsCl (133.5 mM CsCl, 1.8 mM NaCl, 1.7 mM MgCl₂, 0.05 mM EGTA, 10 mM HEPES, 2
789 mM Mg-ATP, 0.4 mM Na₂-GTP, 10 mM phosphocreatine, and 8 mM biocytin, pH: 7.2; 270–290 mOsm). To
790 investigate isolated excitatory or inhibitory events, 5 μM SR 95531 hydrobromide (6-Imino-3-(4-methoxyphenyl)-
791 1(6H)-pyridazinebutanoic acid hydrobromide) or 10 μM CNQX (6-Cyano-7-nitroquinoxaline-2,3-dione) and 20
792 μM D-AP5 (D-(-)-2-Amino-5-phosphonopentanoic acid) was added, respectively. At the end of these recordings,
793 the identity of the recorded synaptic events was confirmed by the application of the above mentioned specific
794 antagonists. These recordings showed no significant difference in the amplitude of excitatory events in TOR and
795 RS cells (TOR: $-43.4 \pm 0.6 \text{ pA}$, RS: $-41.6 \pm 0.4 \text{ pA}$, *Mann-Whitney test*; $p = 0.1398$, $U = 3.42002 \cdot 106$, $Z = 1.47654$).
796 The simulated excitatory conductances corresponded to these events as their magnitude followed a normal
797 distribution (mean: 0.22 nS, variance: 0.01 nS). The simulated inhibitory conductance represented both tonic and
798 phasic inhibition (model distribution mean: 2 nS, variance: 0.1 nS) and was based on the similar inhibitory events
799 recorded in CCK+INs (TOR: $-89.1 \pm 1.4 \text{ pA}$, RS: $-78.1 \pm 1.7 \text{ pA}$). Synaptic conductances were distributed along
800 the dendrites and somatas of the simulated cells uniformly. In the final model, inhibitory conductances followed a
801 uniform random temporal distribution, whereas excitatory events were aggregated into normal distributions
802 packages at various frequencies to recreating *in vivo* relevant MP oscillations in single cells, as follows:

803
$$onset_{Glut} = \frac{1000}{freq} * 0.633 + \left(69.25112 * (0.67747^{freq}) \right) + \frac{1000}{freq}$$

804 where $onset_{Glut}$ is the timing of an individual excitatory event, and $freq$ is the frequency by which excitatory packages
805 occur. This equation is necessary for setting the width of each normal distribution according to the desired
806 frequency, and therefore keeping the sinusoid shape of the MP during the simulated oscillations. In these
807 simulations, 20 oscillatory cycles or in case of high frequencies at least 5 second simulation times were used. Before
808 each run, excitatory and inhibitory event amplitudes and onsets were randomized in a unique but reproducible
809 manner (pseudo-randomization with seed value). If the RS model ($I_{SA}RS$) elicited APs, simulations were repeated
810 with TOR model ($I_{SA}TOR+RS$). The amount of excitation was set to produce firing frequencies below 50 Hz in RS
811 cells. Changes in firing rate caused by the replacement of $I_{SA}RS$ with $I_{SA}TOR+RS$ was calculated by subtraction of
812 the TOR firing rate from RS firing rate and normalized to the latter. Simulations were run on the Neuroscience
813 Gateway (Sivagnanam et al., 2015).

814 **Data analysis and statistics** Data was analysed using Molecular Devices pClamp, OriginLab Origin, Microsoft
815 Excel software and Python-based scripts. Normality of the data was analyzed with Shapiro-Wilks test. Data are
816 presented as mean \pm s.e.m.

817

818 Acknowledgement

819 We thank Professors Henry Jerng, Paul Pfaffinger and Tõnis Timmusk for advices on DPP6 and KChIP isoforms.
820 We are thankful for the computational resources provided by the Neuroscience Gateway. We thank Andrea Szabó,
821 Dóra Rónaszéki, Dóra Kókay and Andrea Juszel for their their excellent technical assistance and László Barna for
822 the kindly provided microscopy support at the Nikon Microscopy Center at the IEM HAS, which is sponsored by
823 Nikon Europe, Nikon Austria and Auro-Science Consulting. This work was supported by Wellcome Trust
824 International Senior Research Fellowship 087497, Hungarian Brain Research Program KTIA_13_NAP-A-I/5,
825 European Research Council Consolidator Grant (772452, nanoAXON) to J.S., Stephen W. Kuffler Research
826 Foundation to V.J.O., Swiss National Science Foundation (CRETP3_166815 and 31003A_170085) and from the
827 Slack-Gyr Foundation to C.F.. ZN is the recipient of a Hungarian National Research Development and Innovation
828 Office collaborative research grant (VKSz 14-1-2015-0155), a European Research Council Advanced Grant, and a
829 Hungarian National Brain Research Program (NAP2.0) grant.

830 References

- BECK, E. J., BOWLBY, M., AN, W. F., RHODES, K. J. & COVARRUBIAS, M. 2002. Remodellin inactivation gating of Kv4 channels by KChIP1, a small-molecular-weight calcium-binding protein. *J Physiol*, 538, 691-706.
- BEZAIRE, M. J., RAIKOV, I., BURK, K., VYAS, D. & SOLTESZ, I. 2016. Interneuronal mechanisms of hippocampal theta oscillations in a full-scale model of the rodent CA1 circuit. *Elife*, 5.
- BOURDEAU, M. L., LAPLANTE, I., LAURENT, C. E. & LACAILLE, J. C. 2011. KChIP1 modulation of Kv4.3-mediated A-type K(+) currents and repetitive firing in hippocampal interneurons. *Neuroscience*, 176, 173-87.
- BOURDEAU, M. L., MORIN, F., LAURENT, C. E., AZZI, M. & LACAILLE, J. C. 2007. Kv4.3-mediated A-type K+ currents underlie rhythmic activity in hippocampal interneurons. *J Neurosci*, 27, 1942-53.
- CEA-DEL RIO, C. A., LAWRENCE, J. J., ERDELYI, F., SZABO, G. & MCBAIN, C. J. 2011. Cholinergic modulation amplifies the intrinsic oscillatory properties of CA1 hippocampal cholecystokinin-positive interneurons. *J Physiol*, 589, 609-27.
- CLOSE, J., XU, H., DE MARCO GARCIA, N., BATISTA-BRITO, R., ROSSIGNOL, E., RUDY, B. & FISHELL, G. 2012. Satb1 is an activity-modulated transcription factor required for the terminal differentiation and connectivity of medial ganglionic eminence-derived cortical interneurons. *J Neurosci*, 32, 17690-705.
- COPE, D. W., MACCAFERRI, G., MARTON, L. F., ROBERTS, J. D., COBDEN, P. M. & SOMOGYI, P. 2002. Cholecystokinin-immunopositive basket and Schaffer collateral-associated interneurons target different domains of pyramidal cells in the CA1 area of the rat hippocampus. *Neuroscience*, 109, 63-80.
- DESIMONE, C. V., ZARAYSKIY, V. V., BONDARENKO, V. E. & MORALES, M. J. 2011. Heteropoda toxin 2 interaction with Kv4.3 and Kv4.1 reveals differences in gating modification. *Mol Pharmacol*, 80, 345-55.
- FÖLDY, C., DARMANIS, S., AOTO, J., MALENKA, R. C., QUAKE, S. R. & SUDHOF, T. C. 2016. Single-cell RNAseq reveals cell adhesion molecule profiles in electrophysiologically defined neurons. *Proc Natl Acad Sci U S A*, 113, E5222-31.
- FREUND, T. F. & BUZSAKI, G. 1996. Interneurons of the hippocampus. *Hippocampus*, 6, 347-470.
- FREUND, T. F. & KATONA, I. 2007. Perisomatic inhibition. *Neuron*, 56, 33-42.
- FUZZIK, J., ZEISEL, A., MATE, Z., CALVIGIONI, D., YANAGAWA, Y., SZABO, G., LINNARSSON, S. & HARKANY, T. 2016. Integration of electrophysiological recordings with single-cell RNA-seq data identifies neuronal subtypes. *Nat Biotechnol*, 34, 175-183.
- GENTET, L. J., STUART, G. J. & CLEMENTS, J. D. 2000. Direct measurement of specific membrane capacitance in neurons. *Biophys J*, 79, 314-20.
- GLICKFELD, L. L. & SCANZIANI, M. 2006. Distinct timing in the activity of cannabinoid-sensitive and cannabinoid-insensitive basket cells. *Nat Neurosci*, 9, 807-15.
- HARRIS, K. D., HOCHGERNER, H., SKENE, N. G., MAGNO, L., KATONA, L., BENGTSSON GONZALES, C., SOMOGYI, P., KESSARIS, N., LINNARSSON, S. & HJERLING-LEFFLER, J. 2018. Classes and continua of hippocampal CA1 inhibitory neurons revealed by single-cell transcriptomics. *PLoS Biol*, 16, e2006387.
- HENDRY, S. H. & JONES, E. G. 1985. Morphology of synapses formed by cholecystokinin-immunoreactive axon terminals in regio superior of rat hippocampus. *Neuroscience*, 16, 57-68.
- HOLMQVIST, M. H., CAO, J., HERNANDEZ-PINEDA, R., JACOBSON, M. D., CARROLL, K. I., SUNG, M. A., BETTY, M., GE, P., GILBRIDE, K. J., BROWN, M. E., JURMAN, M. E., LAWSON, D., SILOS-SANTIAGO, I., XIE, Y., COVARRUBIAS, M., RHODES, K. J., DISTEFANO, P. S. & AN, W. F. 2002. Elimination of fast inactivation in Kv4 A-type potassium channels by an auxiliary subunit domain. *Proc Natl Acad Sci U S A*, 99, 1035-40.
- HU, H., GAN, J. & JONAS, P. 2014. Interneurons. Fast-spiking, parvalbumin(+) GABAergic interneurons: from cellular design to microcircuit function. *Science*, 345, 1255263.
- JERNG, H. H., KUNJILWAR, K. & PFAFFINGER, P. J. 2005. Multiprotein assembly of Kv4.2, KChIP3 and DPP10 produces ternary channel complexes with ISA-like properties. *J Physiol*, 568, 767-88.

- JERNG, H. H., LAUVER, A. D. & PFAFFINGER, P. J. 2007. DPP10 splice variants are localized in distinct neuronal populations and act to differentially regulate the inactivation properties of Kv4-based ion channels. *Mol Cell Neurosci*, 35, 604-24.
- JERNG, H. H. & PFAFFINGER, P. J. 2008. Multiple Kv channel-interacting proteins contain an N-terminal transmembrane domain that regulates Kv4 channel trafficking and gating. *J Biol Chem*, 283, 36046-59.
- JERNG, H. H. & PFAFFINGER, P. J. 2012. Incorporation of DPP6a and DPP6K variants in ternary Kv4 channel complex reconstitutes properties of A-type K current in rat cerebellar granule cells. *PLoS One*, 7, e38205.
- JERNG, H. H. & PFAFFINGER, P. J. 2014. Modulatory mechanisms and multiple functions of somatodendritic A-type K (+) channel auxiliary subunits. *Front Cell Neurosci*, 8, 82.
- KLAUSBERGER, T., MARTON, L. F., O'NEILL, J., HUCK, J. H., DALEZIOS, Y., FUENTEALBA, P., SUEN, W. Y., PAPP, E., KANEKO, T., WATANABE, M., CSICSVARI, J. & SOMOGYI, P. 2005. Complementary roles of cholecystinin- and parvalbumin-expressing GABAergic neurons in hippocampal network oscillations. *J Neurosci*, 25, 9782-93.
- KLAUSBERGER, T. & SOMOGYI, P. 2008. Neuronal diversity and temporal dynamics: the unity of hippocampal circuit operations. *Science*, 321, 53-7.
- KOLLO, M., HOLDERITH, N. B. & NUSSER, Z. 2006. Novel subcellular distribution pattern of A-type K⁺ channels on neuronal surface. *J Neurosci*, 26, 2684-91.
- LAMMEL, S., HETZEL, A., HACKEL, O., JONES, I., LISS, B. & ROEPER, J. 2008. Unique properties of mesoprefrontal neurons within a dual mesocorticolimbic dopamine system. *Neuron*, 57, 760-73.
- LASZTOCZI, B., TUKKER, J. J., SOMOGYI, P. & KLAUSBERGER, T. 2011. Terminal field and firing selectivity of cholecystinin-expressing interneurons in the hippocampal CA3 area. *J Neurosci*, 31, 18073-93.
- LIEN, C. C., MARTINA, M., SCHULTZ, J. H., EHMKE, H. & JONAS, P. 2002. Gating, modulation and subunit composition of voltage-gated K(+) channels in dendritic inhibitory interneurons of rat hippocampus. *J Physiol*, 538, 405-19.
- MARDER, E. & GOAILLARD, J. M. 2006. Variability, compensation and homeostasis in neuron and network function. *Nat Rev Neurosci*, 7, 563-74.
- MARGRIE, T. W., SAKMANN, B. & URBAN, N. N. 2001. Action potential propagation in mitral cell lateral dendrites is decremental and controls recurrent and lateral inhibition in the mammalian olfactory bulb. *Proceedings of the National Academy of Sciences of the United States of America*, 98, 319-324.
- MATYAS, F., FREUND, T. F. & GULYAS, A. I. 2004. Convergence of excitatory and inhibitory inputs onto CCK-containing basket cells in the CA1 area of the rat hippocampus. *Eur J Neurosci*, 19, 1243-56.
- NADAL, M. S., AMARILLO, Y., VEGA-SAENZ DE MIERA, E. & RUDY, B. 2006. Differential characterization of three alternative spliced isoforms of DPPX. *Brain Res*, 1094, 1-12.
- NADAL, M. S., OZAITA, A., AMARILLO, Y., VEGA-SAENZ DE MIERA, E., MA, Y., MO, W., GOLDBERG, E. M., MISUMI, Y., IKEHARA, Y., NEUBERT, T. A. & RUDY, B. 2003. The CD26-related dipeptidyl aminopeptidase-like protein DPPX is a critical component of neuronal A-type K⁺ channels. *Neuron*, 37, 449-61.
- NEUBRANDT, M., OLAH, V. J., BRUNNER, J., MAROSI, E. L., SOLTESZ, I. & SZABADICS, J. 2018. Single Bursts of Individual Granule Cells Functionally Rearrange Feedforward Inhibition. *J Neurosci*, 38, 1711-1724.
- NEUHOFF, H., NEU, A., LISS, B. & ROEPER, J. 2002. I(h) channels contribute to the different functional properties of identified dopaminergic subpopulations in the midbrain. *J Neurosci*, 22, 1290-302.
- NUSSER, Z. 2009. Variability in the subcellular distribution of ion channels increases neuronal diversity. *Trends Neurosci*, 32, 267-74.
- OVERSTREET-WADICHE, L. & MCBAIN, C. J. 2015. Neurogliaform cells in cortical circuits. *Nat Rev Neurosci*, 16, 458-68.
- PENG, H., RUAN, Z., LONG, F., SIMPSON, J. H. & MYERS, E. W. 2010. V3D enables real-time 3D visualization and quantitative analysis of large-scale biological image data sets. *Nat Biotechnol*, 28, 348-53.
- PONGS, O. & SCHWARZ, J. R. 2010. Ancillary subunits associated with voltage-dependent K⁺ channels. *Physiol Rev*, 90, 755-96.

- PRUUNSILD, P. & TIMMUSK, T. 2012. Subcellular localization and transcription regulatory potency of KCNIP/Calsenilin/DREAM/KChIP proteins in cultured primary cortical neurons do not provide support for their role in CRE-dependent gene expression. *J Neurochem*, 123, 29-43.
- QUE, L., WINTERER, J. & FÖLDY, C. 2019. Deep Survey of GABAergic Interneurons: Emerging Insights From Gene-Isoform Transcriptomics. *Front Mol Neurosci*, 12, 115.
- RHODES, K. J., CARROLL, K. I., SUNG, M. A., DOLIVEIRA, L. C., MONAGHAN, M. M., BURKE, S. L., STRASSLE, B. W., BUCHWALDER, L., MENEGOLA, M., CAO, J., AN, W. F. & TRIMMER, J. S. 2004. KChIPs and Kv4 alpha subunits as integral components of A-type potassium channels in mammalian brain. *J Neurosci*, 24, 7903-15.
- SANGUINETTI, M. C., JOHNSON, J. H., HAMMERLAND, L. G., KELBAUGH, P. R., VOLKMANN, R. A., SACCOMANO, N. A. & MUELLER, A. L. 1997. Heteropodatoxins: peptides isolated from spider venom that block Kv4.2 potassium channels. *Mol Pharmacol*, 51, 491-8.
- SEIKEL, E. & TRIMMER, J. S. 2009. Convergent modulation of Kv4.2 channel alpha subunits by structurally distinct DPPX and KChIP auxiliary subunits. *Biochemistry*, 48, 5721-30.
- SIVAGNANAM, S., MAJUMDAR, A., YOSHIMOTO, K., ASTAKHOV, V., BANDROWSKI, A., MARTONE, M. & CARNEVALE, N. T. 2015. Early experiences in developing and managing the neuroscience gateway. *Concurr Comput*, 27, 473-488.
- SOMOGYI, J., BAUDE, A., OMORI, Y., SHIMIZU, H., EL MESTIKAWY, S., FUKAYA, M., SHIGEMOTO, R., WATANABE, M. & SOMOGYI, P. 2004. GABAergic basket cells expressing cholecystokinin contain vesicular glutamate transporter type 3 (VGLUT3) in their synaptic terminals in hippocampus and isocortex of the rat. *Eur J Neurosci*, 19, 552-69.
- STERN, J. E. & ARMSTRONG, W. E. 1996. Changes in the electrical properties of supraoptic nucleus oxytocin and vasopressin neurons during lactation. *J Neurosci*, 16, 4861-71.
- SZABADICS, J. & SOLTESZ, I. 2009. Functional specificity of mossy fiber innervation of GABAergic cells in the hippocampus. *J Neurosci*, 29, 4239-51.
- SZABO, G. G., PAPP, O. I., MATE, Z., SZABO, G. & HAJOS, N. 2014. Anatomically heterogeneous populations of CB1 cannabinoid receptor-expressing interneurons in the CA3 region of the hippocampus show homogeneous input-output characteristics. *Hippocampus*, 24, 1506-23.
- TANG, Y. Q., LIANG, P., ZHOU, J., LU, Y., LEI, L., BIAN, X. & WANG, K. 2013. Auxiliary KChIP4a suppresses A-type K⁺ current through endoplasmic reticulum (ER) retention and promoting closed-state inactivation of Kv4 channels. *J Biol Chem*, 288, 14727-41.
- TANG, Y. Q., ZHOU, J. H., YANG, F., ZHENG, J. & WANG, K. 2014. The tetramerization domain potentiates Kv4 channel function by suppressing closed-state inactivation. *Biophys J*, 107, 1090-1104.
- TASIC, B. 2018. Single cell transcriptomics in neuroscience: cell classification and beyond. *Curr Opin Neurobiol*, 50, 242-249.
- VIDA, I. & FROTSCHER, M. 2000. A hippocampal interneuron associated with the mossy fiber system. *Proc Natl Acad Sci U S A*, 97, 1275-80.
- VIDA, I., HALASY, K., SZINYEI, C., SOMOGYI, P. & BUHL, E. H. 1998. Unitary IPSPs evoked by interneurons at the stratum radiatum-stratum lacunosum-moleculare border in the CA1 area of the rat hippocampus in vitro. *J Physiol*, 506 (Pt 3), 755-73.
- ZEISEL, A., MUNOZ-MANCHADO, A. B., CODELUPPI, S., LONNERBERG, P., LA MANNO, G., JUREUS, A., MARQUES, S., MUNGUBA, H., HE, L., BETSHOLTZ, C., ROLNY, C., CASTELO-BRANCO, G., HJERLING-LEFFLER, J. & LINNARSSON, S. 2015. Brain structure. Cell types in the mouse cortex and hippocampus revealed by single-cell RNA-seq. *Science*, 347, 1138-42.
- ZHOU, J., TANG, Y., ZHENG, Q., LI, M., YUAN, T., CHEN, L., HUANG, Z. & WANG, K. 2015. Different KChIPs compete for heteromultimeric assembly with pore-forming Kv4 subunits. *Biophys J*, 108, 2658-69.